

# DPP9 sequesters the C terminus of NLRP1 to repress inflammasome activation

<https://doi.org/10.1038/s41586-021-03350-4>

Received: 13 August 2020

Accepted: 9 February 2021

Published online: 17 March 2021

 Check for updates

L. Robert Hollingsworth<sup>1,2,3,8</sup>, Humayun Sharif<sup>1,2,8</sup>, Andrew R. Griswold<sup>4,5,8</sup>, Pietro Fontana<sup>1,2</sup>, Julian Mintseris<sup>6</sup>, Kevin B. Dagbay<sup>1,2</sup>, Joao A. Paulo<sup>6</sup>, Steven P. Gygi<sup>6</sup>, Daniel A. Bachovchin<sup>5,7</sup>✉ & Hao Wu<sup>1,2</sup>✉

Nucleotide-binding domain and leucine-rich repeat pyrin-domain containing protein 1 (NLRP1) is an inflammasome sensor that mediates the activation of caspase-1 to induce cytokine maturation and pyroptosis<sup>1–4</sup>. Gain-of-function mutations of *NLRP1* cause severe inflammatory diseases of the skin<sup>4–6</sup>. NLRP1 contains a function-to-find domain that auto-proteolyzes into noncovalently associated subdomains<sup>7–9</sup>, and proteasomal degradation of the repressive N-terminal fragment of NLRP1 releases its inflammatory C-terminal fragment (NLRP1 CT)<sup>10,11</sup>. Cytosolic dipeptidyl peptidases 8 and 9 (hereafter, DPP8/DPP9) both interact with NLRP1, and small-molecule inhibitors of DPP8/DPP9 activate NLRP1 by mechanisms that are currently unclear<sup>10,12–14</sup>. Here we report cryo-electron microscopy structures of the human NLRP1–DPP9 complex alone and with Val-boroPro (VbP), an inhibitor of DPP8/DPP9. The structures reveal a ternary complex that comprises DPP9, full-length NLRP1 and the NLRP1 CT. The binding of the NLRP1 CT to DPP9 requires full-length NLRP1, which suggests that NLRP1 activation is regulated by the ratio of NLRP1 CT to full-length NLRP1. Activation of the inflammasome by ectopic expression of the NLRP1 CT is consistently rescued by co-expression of autoproteolysis-deficient full-length NLRP1. The N terminus of the NLRP1 CT inserts into the DPP9 active site, and VbP disrupts this interaction. Thus, VbP weakens the NLRP1–DPP9 interaction and accelerates degradation of the N-terminal fragment<sup>10</sup> to induce inflammasome activation. Overall, these data demonstrate that DPP9 quenches low levels of NLRP1 CT and thus serves as a checkpoint for activation of the NLRP1 inflammasome.

NLRP1 senses danger-associated signals that cause protein destabilization and/or degradation, such as direct cleavage and ubiquitination by microbial proteases and ubiquitin ligases, respectively<sup>3,4</sup>. Recent studies have demonstrated that functional degradation of the N-terminal fragment of NLRP1 by the proteasome is a mechanism for activation of NLRP1<sup>10,11</sup>. Because auto-proteolysis of the function-to-find domain (FIIND) creates a break in the NLRP1 polypeptide chain between the ZU5 and UPA subdomains<sup>7,8</sup> (Fig. 1a), degradation of the N-terminal fragment of NLRP1 releases noncovalently associated NLRP1 CT (UPA–CARD) and enables the formation of CARD filaments, the recruitment of apoptosis-associated speck-like protein containing a CARD (ASC) adaptor and of pro-caspase-1, and the activation of caspase-1<sup>10,11</sup>. Active caspase-1 processes pro-cytokines of the interleukin-1 family to their bioactive forms and cleaves gasdermin D (GSDMD) to liberate its pore-forming N terminus, which oligomerizes and perforates cell membranes to mediate cytokine secretion and inflammatory cell death<sup>15</sup>.

In contrast to the selective activation of certain alleles of *NLRP1* by particular microbial effectors, small-molecule inhibitors of DPP8/

DPP9 such as VbP (also known as talabostat or PT-100) activate all functional human and rodent homologues of NLRP1<sup>10,13,14,16,17</sup>. DPP8/DPP9 cleave dipeptides after proline or alanine from the N termini of polypeptides (NH<sub>2</sub>-X-P or NH<sub>2</sub>-X-A, in which X denotes any amino acid)<sup>18,19</sup>, and inhibition of this enzymatic activity accelerates ubiquitination of the N-terminal fragment of NLRP1 and proteasomal degradation via an unknown mechanism<sup>10,12,20,21</sup>. In addition, DPP8/DPP9 bind directly to NLRP1<sup>12,20</sup>, but how DPP8/DPP9 binding modulates activity of the NLRP1 inflammasome remains unclear. Here we sought to address this question through structural studies of the NLRP1–DPP9 complex.

## Cryo-EM structure of the ternary complex

We co-expressed NLRP1 lacking the PYD and CARD domains with DPP9 in mammalian cells, and purified the NLRP1–DPP9 complex to homogeneity (Fig. 1b). We then determined the cryo-electron microscopy (cryo-EM) structure of the NLRP1–DPP9 complex at a resolution of 3.6 Å (Extended Data Fig. 1). We independently validated the atomic

<sup>1</sup>Department of Biological Chemistry and Molecular Pharmacology, Harvard Medical School, Boston, MA, USA. <sup>2</sup>Program in Cellular and Molecular Medicine, Boston Children's Hospital, Boston, MA, USA. <sup>3</sup>Program in Biological and Biomedical Sciences, Harvard Medical School, Boston, MA, USA. <sup>4</sup>Tri-Institutional MD–PhD Program, Weill Cornell Medical College, Rockefeller University and Memorial Sloan Kettering Cancer Center, New York, NY, USA. <sup>5</sup>Pharmacology Program, Weill Cornell Graduate School of Medical Sciences and Memorial Sloan Kettering Cancer Center, New York, NY, USA. <sup>6</sup>Department of Cell Biology, Harvard Medical School, Harvard University, Boston, MA, USA. <sup>7</sup>Chemical Biology Program, Memorial Sloan Kettering Cancer Center, New York, NY, USA. <sup>8</sup>These authors contributed equally: L. Robert Hollingsworth, Humayun Sharif, Andrew R. Griswold. ✉e-mail: bachovcd@msskcc.org; wu@crystal.harvard.edu

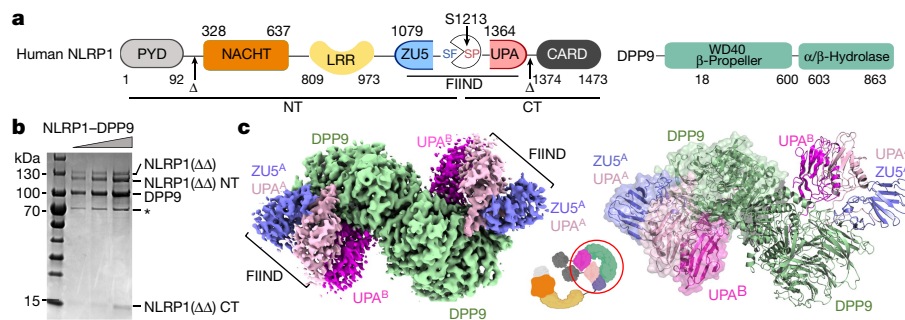


**Fig. 1 | Structure of the NLRP1–DPP9 complex.** **a**, Domain organization. **b**, Representative (of >3 independent experiments) SDS–PAGE of the purified NLRP1–DPP9 complex. HSP70 contamination is noted with an asterisk. NLRP1(ΔΔ), NLRP1 lacking its PYD and CARD domains. **c**, Cryo-EM map (left)

and model (right) of the ternary NLRP1<sup>A</sup>–NLRP1<sup>B</sup>–DPP9 complex. The DPP9 dimer and the two copies of NLRP1 (A and B) are labelled with the colour scheme in **a**. The schematic (middle) denotes the entire NLRP1 and DPP9 molecules versus the ordered, resolved portions of the proteins (red circle).

model using crosslinking mass spectrometry (Extended Data Fig. 2). The cryo-EM structure revealed that two NLRP1 molecules bind to each monomer of the DPP9 dimer, forming an NLRP1<sup>A</sup>–NLRP1<sup>B</sup>–DPP9 ternary complex (in which the superscripts A and B are labels differentiating the two molecules of NLRP1) (Fig. 1c). The first NLRP1 (molecule A) is composed of a complete FIIND along with intimately associated ZU5 and UPA subdomains (Extended Data Fig. 3a–c). The β-sandwich folds in these subdomains are similar to previously defined ZU5 and UPA domains<sup>22,23</sup>, but with a number of differences—in particular, in our structure, the first β-strand (β0) of UPA inserts into the ZU5 fold as if it is the final β-strand of ZU5 (Extended Data Fig. 3b, c). Because our sample contained more autoprocessed NLRP1 than it did unprocessed NLRP1 (Fig. 1b), we built the model as containing processed FIIND. In this model, the catalytic triad residues (S1213 in the UPA domain, and H1186 and E1195 in the ZU5 domain) are nearly correctly positioned for catalysis (Extended Data Fig. 3b), which suggests that the conformational changes between unprocessed and processed forms are probably limited.

The second NLRP1 (molecule B) contains only the UPA subdomain (Fig. 1c). If we place the ZU5 subdomain of the second NLRP1 using the ZU5–UPA structure of the first NLRP1, it clashes with both DPP9 and the first NLRP1 (Extended Data Fig. 3d), which suggests that the second NLRP1 cannot include the ZU5 subdomain or the N-terminal fragment. Thus, the NLRP1<sup>A</sup>–NLRP1<sup>B</sup>–DPP9 complex can only be formed when full-length NLRP1 and N-terminally degraded NLRP1 (that is, NLRP1 CT) are both present. The NACTH and leucine-rich repeat domains of NLRP1 are not visible in the density, probably owing to a flexible linkage between the FIIND and the preceding leucine-rich repeat domain (Fig. 1a).

### NLRP1 CT inserts into the DPP9 tunnel

A notable observation in the NLRP1–DPP9 complex is that the N-terminal segment of UPA<sup>B</sup> (β0; residues S1213 to N1224) unfolds and inserts into the DPP9-substrate tunnel as an extended polypeptide chain (Fig. 2a). The inserted segment in UPA<sup>B</sup> shows a markedly different conformation from that of its UPA<sup>A</sup> counterpart, although the overall conformations of UPA<sup>A</sup> and UPA<sup>B</sup> are similar (Extended Data Fig. 3e, f). Notably, the UPA<sup>B</sup> N terminus (NH<sub>2</sub>-S-P) is a potential substrate for DPP8/DPP9, and the terminal amino group of the segment forms hydrogen-bond and salt-bridge interactions with E248 and E249 in the EE helix of DPP9. The active site of DPP9 is also known to undergo substantial rearrangement at a large loop segment, which partially folds into an α-helix known as the R helix when an arginine residue on the helix engages a substrate<sup>24</sup>. In the NLRP1–DPP9 complex, R133 of DPP9 interacts with main-chain carbonyl oxygen atoms in the N-terminal segment of UPA<sup>B</sup>, and the R helix concomitantly undergoes a disorder-to-order transition (Fig. 2a), similar to substrate or inhibitor binding.

We next explored the structural effect of DPP8/DPP9 inhibitors on the NLRP1–DPP9 complex. We solved a cryo-EM structure of the NLRP1–DPP9 complex purified in the presence of the small-molecule inhibitor VbP (a covalent peptidomimetic that modifies the catalytic S730 of DPP9) at a resolution of 2.9 Å (Fig. 2b, c, Extended Data Figs. 4, 5a). The density of VbP facilitated its unambiguous placement, which showed that VbP interacts with several notable DPP9 residues in addition to the catalytic S730: the R-loop residue R133 and the EE motif composed of E248 and E249 (Fig. 2c, Extended Data Fig. 5b). VbP also induces the substrate-bound state of DPP9, as indicated by ordering of the R helix. In fact, the VbP conformation closely resembles the pose of an isoleucine-proline substrate bound to bacterial DPP4<sup>25</sup> (Extended Data Fig. 5c).

The N-terminal peptide of UPA<sup>B</sup> was absent in the DPP9-substrate tunnel (Fig. 2c), and the entire UPA<sup>B</sup> molecule was weak in the cryo-EM density of the structure of the NLRP1–DPP9–VbP complex (Fig. 2b), which suggests that VbP can displace the NLRP1 CT from DPP9. Superposition of VbP-bound and NLRP1-bound DPP9 structures showed that VbP displaces the NLRP1 CT by direct competition for the active site of DPP9 rather than by causing conformational changes (Extended Data Fig. 5d). Thus, these data rationalize previous reports that VbP weakened the NLRP1–DPP9 interaction, as shown by co-immunoprecipitation and mass spectrometry<sup>12,20</sup>. Despite the binding of the NLRP1 CT to the active site of DPP9 and its displacement by VbP, DPP9 does not cleave the NLRP1 CT (Extended Data Fig. 6) and probably does not repress activity of the NLRP1 CT by direct dipeptide cleavage.

### Three interfaces mediate complex assembly

There are three interaction sites in the NLRP1<sup>A</sup>–DPP9–NLRP1 CT<sup>B</sup> complex, which we refer to as interface I (primarily between ZU5<sup>A</sup> and DPP9), interface II (between UPA<sup>B</sup> and DPP9) and interface III (between UPA<sup>A</sup> and UPA<sup>B</sup>) (Fig. 2d). For interface I, ZU5<sup>A</sup> (and to a much lesser degree, UPA<sup>A</sup> in the same FIIND) interacts with DPP9; however, UPA<sup>A</sup> helps to recruit NLRP1<sup>B</sup> via interface III. Site A therefore selects for full-length NLRP1 via ZU5<sup>A</sup> at interface I, whereas site B selects for the NLRP1 CT because a theoretical ZU5<sup>B</sup> cannot be accommodated (Extended Data Fig. 3d). All three interfaces are extensive, burying about 1,100 Å<sup>2</sup>, about 1,700 Å<sup>2</sup> and about 900 Å<sup>2</sup> surface area per partner, respectively.

Interface I is formed by the β9 and α1–β5 loop regions in ZU5<sup>A</sup> and the WD40 domain in DPP9, with part of the interactions taking the form of hydrogen bonds between β-strands (Fig. 2e). Part of blade I of DPP9 is disordered in the DPP9 crystal structure<sup>24</sup>, but becomes ordered upon interaction with NLRP1 (Extended Data Fig. 7a). Interface II has two components, one formed by the N-terminal segment of UPA<sup>B</sup> (residues S1213 to N1224), as described in Fig. 2a, and the

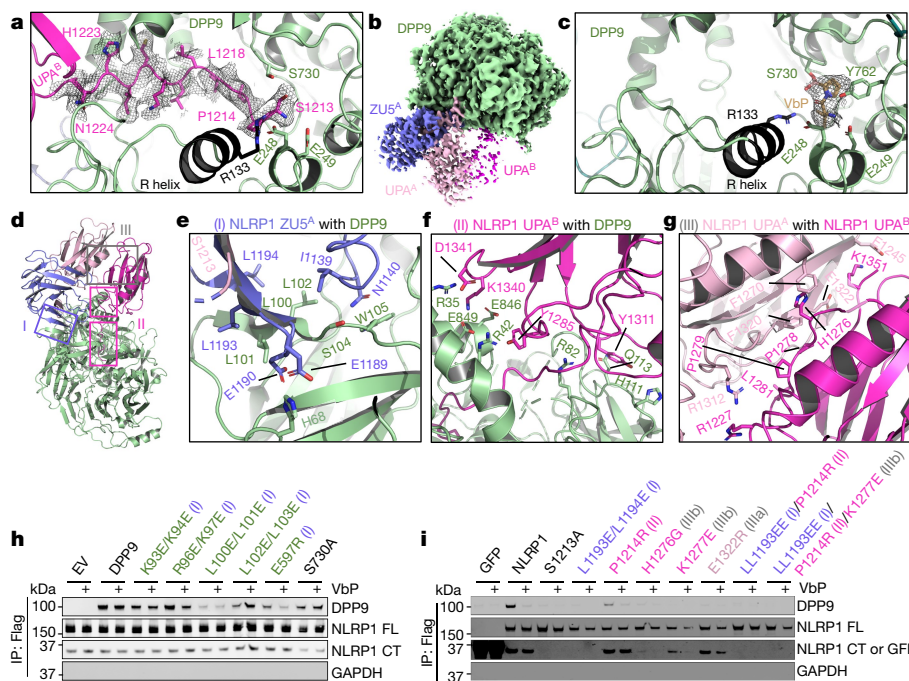


**Fig. 2 | Detailed interfaces in the NLRP1–DPP9 ternary complex and inhibition by VbP.** **a**, Insertion of the N-terminal peptide of UPA<sup>B</sup> into the DPP9 active site. **b**, Cryo-EM map of the NLRP1–DPP9 complex in the presence of VbP. VbP binding reduces UPA<sup>B</sup> occupancy. **c**, Displacement of the UPA<sup>B</sup> N-terminal peptide from the DPP9 active site by VbP. **d**, Overview of three interfaces important for the association between NLRP1 and DPP9. Outlined regions are shown in detail in **a**, **e–g**. **e–g**, Close-up views of each NLRP1–DPP9 binding interface. **h**, Flag co-immunoprecipitation using Flag-tagged wild-type (WT)

NLRP1 and the indicated His-tagged DPP9 constructs expressed in *DPP8DPP9* double-knockout HEK293T cells. EV, empty vector; IP, immunoprecipitate. **i**, Flag co-immunoprecipitation using Flag-tagged NLRP1 (NLRP1–Flag) expressed in HEK293T cells. Flag-tagged GFP was used as a negative control. LL1193EE denotes L1193E/L1194E. The Roman numerals in parentheses in **h**, **i** denote the three interfaces in the NLRP1–DPP9 ternary complex. Each immunoblot is representative of >2 independent experiments.

other formed between one face of the UPA<sup>B</sup> globular domain and the  $\alpha/\beta$ -hydrolase domain of DPP9 (Fig. 2f). In interface III, UPA<sup>A</sup> interacts intimately with UPA<sup>B</sup> using the sides of their  $\beta$ -sandwich folds (Fig. 2g, Extended Data Fig. 3e), comprising both hydrogen-bonding interactions and hydrophobic packing. The relationship between these two UPA subdomains is mainly a translation, and there is only a 9° rotation between them (Extended Data Fig. 3e); to our knowledge, this UPA–UPA interaction has not been observed in other ZU5 and UPA-containing structural homologues<sup>22,23</sup>. Given the translational relationship between these UPA domains, the entire interaction surface differs between UPA<sup>A</sup> and UPA<sup>B</sup> (and we therefore designate these interfaces IIIa and IIIb, respectively).

### Structure-based NLRP1 and DPP9 mutations

We generated structure-based mutations on all three interfaces to determine their effects on the formation of the NLRP1–DPP9 complex. The DPP9(L100E/L101E) or DPP9(E597R) mutant of interface I strongly reduced the interaction with NLRP1 without compromising the post-proline cleavage activity of DPP9 or the sensitivity to VbP (Fig. 2h, Extended Data Fig. 7b–d). We also managed to obtain the NLRP1(L1193E/L1194E) mutant of interface I, which was defective in DPP9 binding and partially defective in FIIND autoprocessing (Fig. 2i, Extended Data Fig. 7e). The interface-II mutant NLRP1(P1214R) at the UPA<sup>B</sup> N terminus (Fig. 2a), a previously described auto-active NLRP1 mutation that causes human disease<sup>12,26</sup>, maintains autoprocessing and showed reduced DPP9 binding (Fig. 2i, Extended Data Fig. 7e). Mutations that affect interface III (the UPA<sup>A</sup> (IIIa)–UPA<sup>B</sup> (IIIb) dimerization surface) abolished DPP9 binding, but retained autoprocessing (Fig. 2i, Extended Data Fig. 7e). Similarly, the NLRP1(S1213A) mutant—which is defective in autoprocessing—or wild-type NLRP1 treated with

VbP also abolished DPP9 binding in the co-immunoprecipitation assay (Fig. 2h, i). These data suggest that there is cooperativity between the two NLRP1 molecules in binding DPP9, in which neither full-length NLRP1<sup>A</sup> nor NLRP1 CT<sup>B</sup> binds to DPP9 without the other. However, in vitro, the high protein concentration could facilitate the binding of full-length NLRP1<sup>A</sup> to DPP9 even when NLRP1 CT<sup>B</sup> is largely absent (Fig. 2b).

### Interface I and II mutations cause auto-activation

Because inhibition or genetic ablation of DPP9 activates NLRP1<sup>12,14,17</sup>, we hypothesized that the loss of the interaction with DPP9 would result in auto-activation of NLRP1. We designed a system using HEK293T cells that recapitulates key components of the inflammasome pathway to evaluate the functional consequences of specifically disrupting interactions between full-length NLRP1<sup>A</sup>, NLRP1 CT<sup>B</sup> or both and DPP9. Specifically, we transiently reconstituted NLRP1 mutants in which the interaction with DPP9 is lost and ASC in HEK293T cells that stably express caspase-1 and GSDMD, and assayed cell death by measuring the release of the intracellular enzyme lactate dehydrogenase (LDH). Mutations that affect interfaces I and II—including the previously reported P1214R substitution<sup>12,26</sup>—induced marked cell death and GSDMD processing in the absence of VbP, with no further increase upon addition of VbP (Fig. 3a). Similarly, these NLRP1 mutants spontaneously formed ASC specks (Fig. 3b) in the absence of any activating signal. Thus, disruption of interface I or II of NLRP1–DPP9 leads to spontaneous activation of the inflammasome. Notably, despite a large reduction in autoprocessing for the NLRP1(L1193E/L1194E) mutant (Fig. 2i, Extended Data Fig. 7e), this construct was still auto-active (Fig. 3a, b), which suggests that only a small amount of free NLRP1 CT is required for inflammasome activity.

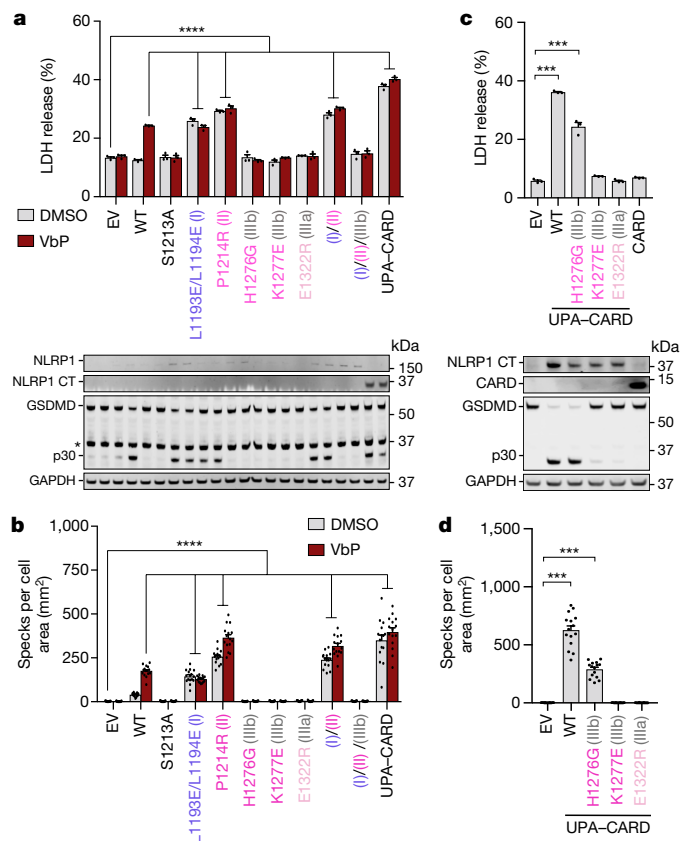


**Fig. 3 | Functional consequences of mutations that affect assembly of the NLRP1-DPP9 ternary complex.** Mutants in which interfaces I and II are affected cause NLRP1 auto-activation, and UPA-UPA interactions are required for inflammasome activity. **a**, LDH release (top) and GSDMD processing (bottom) from transient expression of indicated constructs in a reconstituted HEK293T inflammasome system, with and without addition of VbP.  $n = 3$  independent biological replicates. Asterisks denote nonspecific bands; p30, GSDMD N-terminal fragment from caspase-1 cleavage. I/II denotes NLRP1(LL1193EE/P1214R); I/II/IIb denotes NLRP1(LL1193EE/P1214R/K1277E). **b**, Quantification of speck formation induced by expression of indicated constructs in the presence and absence of VbP.  $n = 15$  quantified fields of view. **c**, LDH release (top) and GSDMD processing (bottom) by direct expression of wild-type or mutant NLRP1 UPA-CARD. CARD alone was also included.  $n = 3$  independent biological replicates. **d**, Quantification of speck formation induced by expression of wild-type or mutant NLRP1 UPA-CARD.  $n = 15$  quantified fields of view. All data are representative of  $>3$  independent experiments. \*\*\*\* $P < 0.0001$  compared to empty vector by two-way analysis of variance (ANOVA) with Tukey's multiple-comparison correction (**a**, **b**). \*\*\* $P < 0.001$  by unpaired two-sided  $t$ -test (**c**, **d**). Exact  $P$  values are provided in Source Data. Data in **a-d** are mean  $\pm$  s.e.m.

### Interface III mutations abolish activity

Mutants in which there was a loss of interaction between UPA<sup>A</sup> and UPA<sup>B</sup> (that is, affecting interface III) were completely deficient in both spontaneous and VbP-mediated inflammasome signalling (Fig. 3a, b), despite their retention of some autoproteolysis (Fig. 2i). Furthermore, addition of the K1277E mutation that disrupted interface III abolished the auto-activation of a mutant in which both interface I and interface II were affected (Fig. 3a, b). As it has recently been demonstrated that the UPA subdomain promotes the formation of CARD filaments and NLRP1 inflammasome signalling<sup>27,28</sup> through self-oligomerization, we reasoned that this function is driven by interface-III interactions. To test this hypothesis, we ectopically expressed the NLRP1 CT in our reconstituted HEK293T cell system, which—as expected—induced cell

death and the formation of ASC specks (Fig. 3c, d). The mutations that affected interface III abolished or reduced cell death, GSDMD cleavage and the formation of ASC specks mediated by NLRP1 CT (Fig. 3c, d). A construct comprising only the CARD of NLRP1 was similarly deficient in inducing cell death (Fig. 3c). This requirement for the UPA domain and the UPA-UPA interface-III contacts in activation of the inflammasome by NLRP1 CT suggests that UPA has an architectural role in inflammasome assembly.

The UPA within an intact FIIND cannot self-oligomerize owing to clashes with ZU5 (Extended Data Figs. 3d, 8a). In addition, freed NLRP1 CT cannot be further recruited to the ternary complex by an UPA-UPA interaction with either UPA<sup>A</sup> (owing to a clash with ZU5<sup>A</sup>) or with UPA<sup>B</sup> (owing to clashes with both monomers of the DPP9 dimer) (Extended Data Fig. 8b). However, the UPA domains in freed NLRP1 CT could—in principle—oligomerize, assuming that they maintain the same near front-to-back binding mode that is seen in the complex with DPP9 (Extended Data Fig. 8c, d). This UPA oligomerization would create a platform for CARD oligomerization, ASC recruitment and inflammasome assembly. Thus, UPA oligomerization has two opposing functions: to mediate repression of the NLRP1 CT through associations with DPP9 and to facilitate inflammasome activation by promoting CARD oligomerization.

### DPP9 sequesters NLRP1 CT with full-length NLRP1

Because mutations on either side of the UPA<sup>A</sup>-UPA<sup>B</sup> interface disrupted the association between NLRP1 and DPP9, but retained autoproteolysis (Fig. 2i), we reasoned that DPP9 binding by full-length NLRP1 and NLRP1 CT is cooperative, and that full-length NLRP1 might dimerize with NLRP1 CT. We co-expressed Flag-tagged NLRP1(S1213A), which is auto-proteolytically deficient and can occupy only site A, with a construct for NLRP1 CT that can occupy only site B. For expression of NLRP1 CT, we used an N-terminal ubiquitin (Ub) fusion (Ub-NLRP1 CT), which is co-translationally processed<sup>29,30</sup> to generate the native N terminus (that is, with serine at position 1213) (Fig. 4a). NLRP1(S1213A) captured NLRP1 CT, and co-expression of these two components rescued association with DPP9 (Fig. 4b), which directly confirms that DPP9 engagement is cooperative. The addition of DPP8/DPP9 inhibitors to this preformed ternary complex in lysates (Fig. 4b) or on beads (Extended data Fig. 9a, b) displaced DPP9, as expected. By contrast, DPP8/DPP9 inhibitors did not disrupt the interaction between the NLRP1 CT and NLRP1(S1213A), which indicates that dimerization (or oligomerization) can occur in the absence of DPP9 (Fig. 4b, Extended Data Fig. 9a, b). Unlike the NLRP1<sup>A</sup>-NLRP1 CT<sup>B</sup>-DPP9 ternary complex, the NLRP1<sup>A</sup>-NLRP1 CT<sup>B</sup> binary complex should allow UPA-mediated oligomerization on one face of UPA<sup>B</sup>, and should not therefore effectively repress inflammasome formation (Extended Data Fig. 8d).

Because sequestration of NLRP1 CT into the ternary complex should prevent UPA-UPA oligomerization (Extended Data Fig. 8b) and inhibit inflammasome formation, we posited that co-expression of NLRP1(S1213A) and NLRP1 CT would rescue inflammatory cell death mediated by NLRP1 CT through DPP9 association. Indeed, titration of NLRP1(S1213A) reduced cell death mediated by NLRP1 CT in a dose-dependent manner (Fig. 4c). Similarly, a NLRP1 mutant containing only the FIIND domain and with the S1213A substitution (NLRP1(FIIND/S1213A)) reduced the speck formation that resulted from all disease-associated NLRP1 mutations, except for that arising from P1214R (Fig. 4d)—a substitution that impairs the interaction between DPP9 and NLRP1 (Fig. 2i). We next leveraged the degradation tag (dTAG) system to pharmacologically control the release of NLRP1 CT<sup>31</sup>. In brief, we fused FKBP12(F36V) (the dTAG) to the N terminus of NLRP1 (dTAG-NLRP1), and used the small-molecule dTAG13 to recruit the E3 ligase cereblon to the fusion protein and trigger degradation of the N-terminal fragment of NLRP1 (Extended Data Fig. 9c). As expected, dTAG13 robustly induced the degradation and activation of

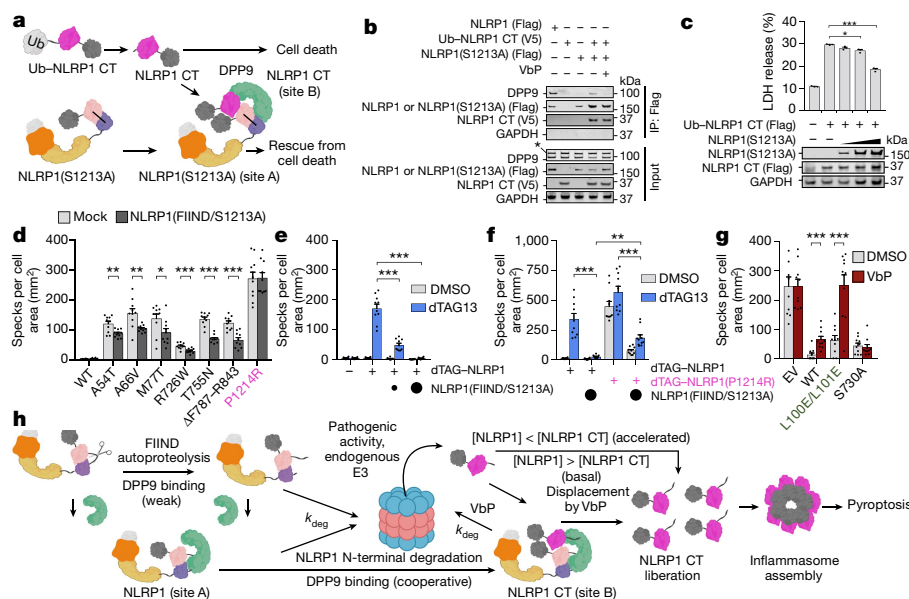


**Fig. 4 | Repression of activity of the NLRP1CT inflammasome by formation of the ternary complex.** **a**, Schematic of ternary complex formation between the autocatalysis-deficient NLRP1(S1213A), Ub-NLRP1 CT and DPP9. Ub-NLRP1 CT is co-translationally processed by endogenous deubiquitinases, resulting in NLRP1 CT with the native N terminus (S1213). **b**, Flag co-immunoprecipitation using Flag-tagged wild-type NLRP1 or NLRP1(S1213A) and V5-tagged Ub-NLRP1 CT. NLRP1(S1213A) (site A) alone did not pull down endogenous DPP9. By contrast, co-expression of the two constructs formed a ternary complex with DPP9. **c**, Increasing amounts of NLRP1(S1213A) suppress NLRP1-CT-induced cell death measured by LDH release in a reconstituted HEK293T inflammasome system.  $n = 3$  independent biological replicates. **d**, NLRP1(FIIND/S1213A) rescues the ASC specks that result from disease-associated NLRP1 mutants, except those resulting from P1214R (which reduces DPP9 binding). **e**, NLRP1(FIIND/S1213A) rescues ASC specks that result from dTAG13-induced degradation of NLRP1. **f**, Formation of ASC specks by

NLRP1(P1214R) and rescue by NLRP1(FIIND/S1213A). NLRP1(FIIND/S1213A) partially rescues dTAG-NLRP1(P1214R), but rescue of dTAG-NLRP1(P1214R) is significantly less than that for dTAG-NLRP1. **g**, DPP9 binding and catalytic activity contribute to repression of the NLRP1 inflammasome. ASC specks from NLRP1 and the indicated DPP9 constructs expressed in *DPP8/DPP9* double-knockout HEK293T cells. In **d–g**,  $n = 10$  quantified fields of view. Data in **c–g** are mean  $\pm$  s.e.m. All data are representative of  $>2$  independent experiments. In **c–d**,  $g$ ,  $*P < 0.05$ ,  $**P < 0.01$ ,  $***P < 0.001$  by unpaired two-sided  $t$ -test. In **e**, **f**,  $***P < 0.01$ ,  $****P < 0.001$  by two-way ANOVA with Tukey's multiple-comparison correction. Exact  $P$  values are provided in Source Data. **h**, Schematic of NLRP1 activation and repression by DPP9. Full-length NLRP1 together with DPP9 represses an as-yet-unknown threshold of free NLRP1 CT. Enhanced N-terminal degradation of full-length NLRP1, or displacement of the NLRP1 CT, leads to inflammasome signalling.

dTAG-NLRP1, as measured by the formation of ASC specks and GSDMD cleavage (Fig. 4e, Extended Data Fig. 9d). Moreover, we observed a dose-dependent rescue of dTAG13-induced activation of the inflammasome with NLRP1(FIIND/S1213A) co-expression (Fig. 4e, Extended Data Fig. 9d). We next tested a dTAG-NLRP1(P1214R) mutant in this system (Fig. 4f), which spontaneously formed ASC specks and was only partially rescued by NLRP1(FIIND/S1213A), consistent with disruption of the binding of NLRP1(P1214R) CT to the repressive ternary complex. Thus, DPP9 represses the inflammatory activity of the NLRP1 CT in a manner that depends on the presence of full-length NLRP1. Finally, we confirmed that both the enzymatic activity and the binding of DPP9 repress NLRP1 activation (Fig. 4g).

## Conclusion

In summary, our structural and cellular data show that full-length NLRP1 and DPP9 act as a checkpoint for activation of the inflammasome by directly binding to and sequestering the inflammatory NLRP1 CT. We propose that free inflammatory NLRP1 CT is not only generated by an (as-yet-unknown) danger-associated signal, but also during normal homeostatic turnover of the protein. Accordingly, the formation of the ternary complex would be needed to avoid spurious inflammation from low background levels of NLRP1 CT relative to NLRP1. It is unclear what happens to these ternary complexes after they are formed, and—in particular—how the inflammatory NLRP1 CT is turned over. As we did not observe cleavage of the NLRP1 CT by DPP9 (Extended Data Fig. 6), we speculate that unknown cellular machinery might recognize the

NLRP1–DPP9 ternary complex and destroy NLRP1 CT, thus preventing its accumulation.

We also considered how cells could overcome this important checkpoint for NLRP1 activation. In one scenario, accelerated degradation of NLRP1 induced by danger-associated signals (for example, pathogen proteases or DPP8/DPP9 inhibition) would lead to a simultaneous increase of NLRP1 CT and decrease of full-length NLRP1 to overwhelm this checkpoint, leading to inflammasome activation and pyroptotic cell death (Fig. 4h). Alternatively, any factor that affects the interaction between NLRP1 and DPP9 (for example, the P1214R substitution in NLRP1 or DPP8/DPP9 inhibitors) would release NLRP1 CT to promote inflammasome activation (Fig. 4h). It is tempting to speculate that additional unknown endogenous- or pathogen-derived signals may act to accelerate the degradation of the N-terminal fragment of NLRP1 and/or alter ternary complex stability, and thereby regulate inflammasome formation. We expect that future studies on the basis of the results presented here will not only lead to greater mechanistic understanding of this inflammasome, but also eventually enable the therapeutic modulation of NLRP1 to treat human disease.

## Online content

Any methods, additional references, Nature Research reporting summaries, source data, extended data, supplementary information, acknowledgements, peer review information; details of author contributions and competing interests; and statements of data and code availability are available at <https://doi.org/10.1038/s41586-021-03350-4>.

1. Martinon, F., Burns, K. & Tschopp, J. The inflammasome: a molecular platform triggering activation of inflammatory caspases and processing of proIL- $\beta$ . *Mol. Cell* **10**, 417–426 (2002).
2. Shen, C., Sharif, H., Xia, S. & Wu, H. Structural and mechanistic elucidation of inflammasome signaling by cryo-EM. *Curr. Opin. Struct. Biol.* **58**, 18–25 (2019).
3. Mitchell, P. S., Sandstrom, A. & Vance, R. E. The NLRP1 inflammasome: new mechanistic insights and unresolved mysteries. *Curr. Opin. Immunol.* **60**, 37–45 (2019).
4. Taabazuing, C. Y., Griswold, A. R. & Bachovchin, D. A. The NLRP1 and CARD8 inflammasomes. *Immunol. Rev.* **297**, 13–25 (2020).
5. Soler, V. J. et al. Whole exome sequencing identifies a mutation for a novel form of corneal intraepithelial dyskeratosis. *J. Med. Genet.* **50**, 246–254 (2013).
6. Zhong, F. L. et al. Germline NLRP1 mutations cause skin inflammatory and cancer susceptibility syndromes via inflammasome activation. *Cell* **167**, 187–202.e17 (2016).
7. D’Osueldo, A. et al. CARD8 and NLRP1 undergo autoproteolytic processing through a ZU5-like domain. *PLoS ONE* **6**, e27396 (2011).
8. Finger, J. N. et al. Autolytic proteolysis within the function to find domain (FIIND) is required for NLRP1 inflammasome activity. *J. Biol. Chem.* **287**, 25030–25037 (2012).
9. Frew, B. C., Joag, V. R. & Mogridge, J. Proteolytic processing of Nlrp1b is required for inflammasome activity. *PLoS Pathog.* **8**, e1002659 (2012).
10. Fingert, A. et al. N-terminal degradation activates the NLRP1B inflammasome. *Science* **364**, 82–85 (2019).
11. Sandstrom, A. et al. Functional degradation: a mechanism of NLRP1 inflammasome activation by diverse pathogen enzymes. *Science* **364**, eaau1330 (2019).
12. Zhong, F. L. et al. Human DPP9 represses NLRP1 inflammasome and protects against autoinflammatory diseases via both peptidase activity and FIIND domain binding. *J. Biol. Chem.* **293**, 18864–18878 (2018).
13. de Vasconcelos, N. M. et al. DPP8/DPP9 inhibition elicits canonical Nlrp1b inflammasome hallmarks in murine macrophages. *Life Sci. Alliance* **2**, e201900313 (2019).
14. Okondo, M. C. et al. Inhibition of Dpp8/9 activates the Nlrp1b inflammasome. *Cell Chem. Biol.* **25**, 262–267.e5 (2018).
15. Xia, S., Hollingsworth, L. R., IV & Wu, H. in *Cell Survival and Cell Death* (eds Newton, K. et al.) Ch. 7 (CSHL Press, 2019).
16. Okondo, M. C. et al. DPP8 and DPP9 inhibition induces pro-caspase-1-dependent monocyte and macrophage pyroptosis. *Nat. Chem. Biol.* **13**, 46–53 (2017).
17. Gai, K. et al. DPP8/9 inhibitors are universal activators of functional NLRP1 alleles. *Cell Death Dis.* **10**, 587 (2019).
18. Griswold, A. R. et al. A chemical strategy for protease substrate profiling. *Cell Chem. Biol.* **26**, 901–907.e6 (2019).
19. Geiss-Friedlander, R. et al. The cytoplasmic peptidase DPP9 is rate-limiting for degradation of proline-containing peptides. *J. Biol. Chem.* **284**, 27211–27219 (2009).
20. Griswold, A. R. et al. DPP9’s enzymatic activity and not its binding to CARD8 inhibits inflammasome activation. *ACS Chem. Biol.* **14**, 2424–2429 (2019).
21. Chui, A. J. et al. Activation of the CARD8 inflammasome requires a disordered region. *Cell Rep.* **33**, 108264 (2020).
22. Wang, R. et al. Autoinhibition of UNC5b revealed by the cytoplasmic domain structure of the receptor. *Mol. Cell* **33**, 692–703 (2009).
23. Wang, C., Yu, C., Ye, F., Wei, Z. & Zhang, M. Structure of the ZU5–ZU5–UPA–DD tandem of ankyrin-B reveals interaction surfaces necessary for ankyrin function. *Proc. Natl Acad. Sci. USA* **109**, 4822–4827 (2012).
24. Ross, B. et al. Structures and mechanism of dipeptidyl peptidases 8 and 9, important players in cellular homeostasis and cancer. *Proc. Natl Acad. Sci. USA* **115**, E1437–E1445 (2018).
25. Roppongi, S. et al. Crystal structures of a bacterial dipeptidyl peptidase IV reveal a novel substrate recognition mechanism distinct from that of mammalian orthologues. *Sci. Rep.* **8**, 2714 (2018).
26. Grandemange, S. et al. A new autoinflammatory and autoimmune syndrome associated with NLRP1 mutations: NAIAD (NLRP1-associated autoinflammation with arthritis and dyskeratosis). *Ann. Rheum. Dis.* **76**, 1191–1198 (2017).
27. Robert Hollingsworth, L. et al. Mechanism of filament formation in UPA-promoted CARD8 and NLRP1 inflammasomes. *Nat. Commun.* **12**, 189 (2021).
28. Gong, Q. et al. Structural basis for distinct inflammasome complex assembly by human NLRP1 and CARD8. *Nat. Commun.* **12**, 188 (2021).
29. Bachmair, A., Finley, D. & Varshavsky, A. In vivo half-life of a protein is a function of its amino-terminal residue. *Science* **234**, 179–186 (1986).
30. Baker, R. T. & Varshavsky, A. Inhibition of the N-end rule pathway in living cells. *Proc. Natl Acad. Sci. USA* **88**, 1090–1094 (1991).
31. Nabet, B. et al. The dTAG system for immediate and target-specific protein degradation. *Nat. Chem. Biol.* **14**, 431–441 (2018).

**Publisher’s note** Springer Nature remains neutral with regard to jurisdictional claims in published maps and institutional affiliations.

© The Author(s), under exclusive licence to Springer Nature Limited 2021

## Methods

No statistical methods were used to predetermine sample size. The experiments were not randomized, and investigators were not blinded to allocation during experiments and outcome assessment.

### Cell culture

Expi293F cells were maintained in Expi293F expression medium (GIBCO, ThermoFisher) with constant shaking at 100 rpm, 37 °C and 5% CO<sub>2</sub>. Sf9 insect cells were maintained in HyClone SFX-insect cell media (Cytiva) supplemented with 1× antibiotic-antimycotic (ThermoFisher) at 27 °C with constant shaking at 100 rpm. HEK293T cell lines and their derivatives were maintained in DMEM (GIBCO, ThermoFisher) supplemented with 10% fetal bovine serum (GIBCO, ThermoFisher Scientific) at 37 °C and 5% CO<sub>2</sub>. HEK293T (ATCC), Sf9 (ThermoFisher) and Expi293F (ThermoFisher) were authenticated by the manufacturer and frequently checked for their morphological features. HEK293T cells stably expressing GSDMD and caspase-1 have previously been described<sup>32</sup>. DPP8 and DPP9 double-knockout HEK293T cells were generated in this study (as described in 'CRISPR-Cas9 gene editing') using previously validated DPP9-knockout cells<sup>20</sup>. Expi293F and Sf9 cells for protein production were not tested regularly for mycoplasma contamination. All other cell lines regularly tested negative for mycoplasma using the MycoAlert Mycoplasma Detection Kit (Lonza).

### Constructs and cloning

Mammalian codon-optimized full-length human NLRP1 cDNA (isoform 1, Uniprot identifier Q9C000-1) was synthesized by Synbio Technologies). Codon-optimized NLRP1 lacking PYD and CARD (residues W148–P1364 (NLRP1(ΔΔ)) was subcloned into an in-house-modified pcDNA3.1 LIC 6D (Addgene plasmid no. 30127) vector containing a C-terminal TEV linker, GFP tag and Flag tag (NLRP1ΔΔ-TEV-GFP-Flag). NLRP1 was also cloned into pcDNA3.1 LIC 6A (Addgene plasmid no. 30124) with a C-terminal Flag tag (NLRP1-Flag). NLRP1 was also subcloned into pDONR221 (Thermo) and shuttled into pLEX 305-N-dTAG (Addgene plasmid no. 91797) with Gateway technology (Thermo). The short isoform of DPP9 (Uniprot identifier Q86TI2-1) from the Harvard PlasmID Database was subcloned into pfastBac HTB (N-terminal His-TEV tag) for recombinant protein expression. DPP9 was then subcloned into pcDNA3.1 LIC 6A with either an N-terminal His or Flag tag (His-TEV-DPP9 or Flag-TEV-DPP9). Point mutations were introduced with Q5 site-directed mutagenesis (NEB) or QuikChange site-directed mutagenesis kit (Agilent). Ub-fused NLRP1 constructs were synthesized (GenScript) with an N-terminal synthetic ubiquitin sequence followed by NLRP1 CT (S1213–S1473, L1215–S1473 or L1218–S1473) and cloned into pcDNA3.1 and pLEX-307 (Addgene plasmid no. 41392) vectors. Study constructs are available on Addgene ([https://www.addgene.org/Hao\\_Wu/](https://www.addgene.org/Hao_Wu/) and [https://www.addgene.org/Daniel\\_Bachovchin/](https://www.addgene.org/Daniel_Bachovchin/)).

### Protein expression, purification, and Edman degradation

Recombinant DPP9 was purified similarly to as previously described<sup>24</sup>. Baculoviruses containing DPP9 were prepared using the Bac-to-Bac system (Invitrogen), and used to generate baculovirus-infected insect cells. To express DPP9, 1 ml of these baculovirus-containing cells was used to infect each litre of Sf9 cells. Cells were collected 48 h after infection by centrifugation (1,682g, 20 min), washed once with phosphate buffered saline (PBS), flash-frozen in liquid nitrogen and stored at –80 °C. The thawed pellet from 2 l of cells was resuspended in lysis buffer (80 ml, 25 mM Tris-HCl pH 8.0, 150 mM NaCl, 1 mM tris(2-carboxyethyl)phosphine (TCEP), 5 mM imidazole), sonicated (3-s on, 5-s off, 3.5 min total on, 45% power, Branson), and ultracentrifuged (186,000g, 1.5 h, 45 Ti fixed-angle rotor, Beckman). After centrifugation, the supernatant was incubated with 1 ml Ni-NTA resin at 4 °C for 1 h. The bound Ni-NTA beads were washed once in batch and subsequently by gravity flow using

50–100 column-volume (CV) wash buffer (25 mM Tris-HCl pH 8.0, 150 mM NaCl, 1 mM TCEP, 25 mM imidazole). The protein was eluted with buffer containing 500 mM imidazole (5 ml), spin-concentrated to 0.5 ml (Amicon Ultra, 100-kDa molecular mass cut-off), and further purified by size-exclusion chromatography (25 mM Tris-HCl pH 7.5, 150 mM NaCl, 1 mM TCEP) on a Superdex 200 increase 10/300 GL column (Cytiva). The yield was about 5 mg l<sup>-1</sup> of insect cell culture.

To purify the NLRP1–DPP9 complex, expi293F cells (1 l, 2–3 × 10<sup>6</sup> cells per ml) were co-transfected with NLRP1ΔΔ-TEV-GFP-Flag (0.7 mg) and the short isoform of DPP9 (His-TEV-DPP9) (0.3 mg) following incubation with polyethylenimine (3 ml, 1 mg ml<sup>-1</sup>) in Opti-MEM (100 ml) for 30 min. Twenty-four hours later, cells were supplemented with glucose (9 ml, 45%) and valproic acid (10 ml, 300 mM). Cells were collected 5 d after transfection by centrifugation (1,329g, 20 min), washed once with PBS, flash-frozen in liquid nitrogen and stored at –80 °C. Later, the thawed pellet from 1 l of cells was resuspended in lysis buffer (50–100 ml, 25 mM Tris-HCl pH 7.5, 150 mM NaCl, 1 mM TCEP), sonicated (2-son, 8-s off, 3.5 min total on, 40% power, Branson), and ultracentrifuged (186,000g, 1 h, 45 Ti fixed-angle rotor, Beckman). The soluble proteome was incubated with pre-equilibrated anti-Flag M2 affinity gel (Sigma, 1.5 ml) for 4 h at 4 °C, washed in batch once with 5–10 CV lysis buffer and then washed by gravity flow with 25–50 CV lysis buffer. The NLRP1–DPP9 complex was eluted by on-column TEV protease cleavage at room temperature for 1 h using elution buffer (5 ml, 25 mM Tris-HCl pH 7.5, 150 mM NaCl, 5 mM MgCl<sub>2</sub>, 0.2 mM ADP, 1 mM TCEP, 0.2 mg TEV protease) and loaded onto a Mono Q 5/50 GL anion exchange column (Cytiva). Protein was eluted using a salt gradient from 150 mM to 1 M NaCl (25 mM Tris-HCl pH 8.0, 1 mM TCEP) over 15 CV. Subsequent purification steps using size-exclusion columns led to complete loss of protein, probably owing to hydrophobic interactions between the protein and the support of the column. Nonetheless, the anion exchange eluent showed sufficiently homogeneous NLRP1–DPP9 complexes by negative-stain electron microscopy. MonoQ eluent containing the complex was concentrated to 0.3–0.5 mg ml<sup>-1</sup> (assuming ε = 1.25) using a 0.5-ml spin concentrator (Amicon Ultra, 50-kDa molecular mass cut-off) and immediately supplemented with 0.2 mM ADP and 5 mM MgCl<sub>2</sub>. Concentrated eluent was dialysed overnight into a HEPES buffer that is compatible with crosslinking for cryo-EM (25 mM HEPES pH 7.5, 150 mM NaCl, 5 mM MgCl<sub>2</sub>, 0.2 mM ADP, 1 mM TCEP) using a 0.5-ml Slide-A-Lyzer (ThermoFisher). Total protein yield varied between 0.2 and 0.5 mg l<sup>-1</sup> of mammalian culture. Purified protein was run on an SDS–PAGE gel, transferred to a PVDF membrane (iBLOT 2), and stained by Coomassie blue. The NLRP1 CT band was excised and sent to the Tufts University Core Facility for Edman degradation.

Expression and purification of the NLRP1–DPP9–VbP complex was identical to that for NLRP1–DPP9, except for the addition of 10 μM VbP to all purification and dialysis buffers. An extended protocol, including intermediary purification and quality control results, is available on protocols.io at <https://www.protocols.io/groups/haowu-lab>.

### Crosslinking mass spectrometry

Amine–amine crosslinking of the purified NLRP1–DPP9 complex was performed at a final concentration of 0.24 mg ml<sup>-1</sup> using either 0.5, 1, or 2 mM bis(sulfosuccinimidyl)suberate (BS3) in 50 mM HEPES pH 7.8 and 100 mM NaCl for 1 h at room temperature. The reaction was quenched with hydroxylamine to a final concentration of 100 mM. Urea was added to 5 M concentration and samples were reduced for 1 h in 10 mM TCEP and 50 mM HEPES pH 8.3, followed by alkylation with 30 mM iodoacetamide in the dark for 1 h and quenching with 50 mM β-mercaptoethanol. Samples were then diluted with 50 mM HEPES pH 8.3 to reduce urea concentration to 1 M and digested with trypsin (Promega) at 1:10 enzyme:substrate ratio overnight at 37 °C. Digested peptides were acidified with 10% formic acid to a pH of about 2, Aesalted using stage tips with Empore C18 SPE extraction discs (3M) and dried under vacuum.

Crosslinked samples were reconstituted in 5% formic acid, 5% acetonitrile, and analysed in the Orbitrap Fusion Lumos mass spectrometer (ThermoFisher) coupled to an EASY-nLC1200 (ThermoFisher) ultra-high pressure liquid chromatography pump, as well as a high-field asymmetric waveform ion mobility spectrometry (FAIMS) FAIMSpro interface. Peptides were separated on an in-house column with 100  $\mu\text{M}$  inner diameter and packed with 35 cm of Accucore C18 resin (2.6  $\mu\text{m}$ , 150  $\text{\AA}$ , ThermoFisher), using a gradient consisting of 5–35% (acetonitrile, 0.125% formic acid) over 135 min at about 500  $\text{nl min}^{-1}$ . The instrument was operated in data-dependent mode. FTMS1 spectra were collected at a resolution of 120,000, with an automatic gain control target of  $5 \times 10^5$ , and a maximum injection time of 50 ms. The most intense ions were selected for tandem mass spectrometry for 1 s in top-speed mode, while switching among three FAIMS compensation voltages (–40, –60, and –80 V) in the same method. Precursors were filtered according to charge state (allowed  $3 \leq z \leq 7$ ), and monoisotopic peak assignment was turned on. Previously investigated precursors were excluded using a dynamic exclusion window of 60 s. MS2 precursors were isolated with a quadrupole mass filter set to a width of 0.7 Th and analysed by FTMS2, with the Orbitrap operating at 30,000 resolution, an automatic gain control target of 100,000 and a maximum injection time of 150 ms. Precursors were then fragmented by high-energy collision dissociation at a 32% normalized collision energy.

Mass spectra were processed and searched using the PIXL search engine<sup>33</sup>. Precursor tolerance was set to 15 ppm and fragment ion tolerance to 10 ppm. Methionine oxidation was set as a variable modification, in addition to mono-linked mass of +156.0786 for BS3. Crosslinker mass shift of +138.0681 was used for BS3 reagent. All crosslinked searches included 50 most abundant protein sequences to ensure sufficient statistics for estimation of the false-discovery rate. Matches were filtered to 1% false-discovery rate on the unique peptide level using linear discriminant features as previously described<sup>33</sup>.

### Cryo-EM grid preparation and data collection

The purified NLRP1–DPP9 complex (0.3–0.5  $\text{mg ml}^{-1}$ , 25 mM HEPES pH 7.5, 150 mM NaCl, 5 mM  $\text{MgCl}_2$ , 0.2 mM ADP, 1 mM TCEP,  $\pm 10 \mu\text{M}$  VbP) was crosslinked with 0.02% glutaraldehyde on ice for 5 min and immediately loaded onto a glow-discharged Quantifoil grid (RI.2/1.3 400-mesh gold-supported holey carbon, Electron Microscopy Sciences), blotted for 3–5 s under 100% humidity at 4  $^\circ\text{C}$  and plunged into liquid ethane using a Mark IV Vitrobot (ThermoFisher). These sample conditions were optimized extensively using insights gleaned from small datasets collected at the Pacific Northwest Center for Cryo-EM (PNCC), the National Cryo-EM Microscope Facility (NCEF) of the NCI and the Harvard Cryo-EM Center (HMS). Final collection parameters are summarized in Extended Data Table 1.

Before data collection, all grids were screened for ice and particle quality. For data collection, movies were acquired at HMS using a Titan Krios microscope (ThermoFisher) at an acceleration voltage of 300 keV equipped with BioQuantum K3 Imaging Filter (Gatan, slit width 20 eV). Movies were recorded with a K3 Summit direct electron detector (Gatan) operating in counting mode at 105,000 $\times$  magnification (0.825  $\text{\AA}$  per pixel).

For the NLRP1–DPP9 dataset at 0 $^\circ$  stage tilt, 7,840 movies were collected using SerialEM<sup>34</sup> to vary the defocus range between –1 and –2.5  $\mu\text{m}$  and to record two shots for each of the four holes per stage movement through image shift. All movies were exposed with a total dose of 67.5  $\text{e}^- \text{per } \text{\AA}^2$  for 1.8 s fractionated over 45 frames. Orientation preference was apparent, and an ideal tilt angle of 37 $^\circ$  was calculated from this processed dataset (as described in ‘Cryo-EM data processing’) using cryoEF<sup>35</sup>. For the NLRP1–DPP9 dataset at a stage tilt of 37 $^\circ$ , 1,916 movies were collected using SerialEM<sup>34</sup> to vary the defocus range between –1.5 and –3.0  $\mu\text{m}$  with two shots recorded for each hole per stage movement through image shift. All movies were exposed with a total dose of 67.6  $\text{e}^- \text{per } \text{\AA}^2$  for 2.6 s fractionated over 45 frames.

For the NLRP1–DPP9–VbP dataset at 0 $^\circ$  stage tilt, 3,553 movies were collected using SerialEM<sup>34</sup> to vary the defocus range between –0.8 and –2.2  $\mu\text{m}$  and to record two shots for each of the four holes per stage movement through image shift. All movies were exposed with a total dose of 52.0  $\text{e}^- \text{per } \text{\AA}^2$  for 2.0 s fractionated over 50 frames. Orientation preference was apparent, and an ideal tilt angle of 37 $^\circ$  was calculated from this processed dataset (as described in ‘Cryo-EM data processing’) using cryoEF<sup>35</sup>. For NLRP1–DPP9–VbP at a stage tilt of 37 $^\circ$ , 1,954 movies were collected using SerialEM<sup>34</sup> to vary the defocus range between –1.5 and –3.0  $\mu\text{m}$  with two shots recorded for each hole per stage movement through image shift. All movies were exposed with a total dose of 65.0  $\text{e}^- \text{per } \text{\AA}^2$  for 2.4 s fractionated over 43 frames.

### Cryo-EM data processing

Our data processing leveraged computer support from the SBGrid Consortium<sup>36</sup> and NSF XSEDE<sup>37</sup> (Extended Data Figs. 1, 4). Movies collected at HMS were pre-processed as they were collected by the in-house pipeline script of the facility. Movies were corrected by gain reference and for beam-induced motion, and summed into motion-corrected images using the Relion 3.08 implementation of the MotionCor2 algorithm<sup>38</sup>. CTFIND4<sup>39</sup> or goCTF<sup>40</sup> was used to determine the defocus of each micrograph (Extended Data Figs. 1, 4). These pre-processed micrographs were used for subsequent analysis.

For the NLRP1–DPP9 complex collected at 0 $^\circ$  stage tilt, crYOLO<sup>41</sup> (generalized training by the HMS facility) picked 1,119,166 particles from the 7,840 micrographs. Relion 3.1<sup>42</sup> was used for subsequent image processing. Initially, picked particles were subjected to several rounds of 2D classification until the classes appeared visually homogenous. A randomized set of 100,000 particles was selected for the de novo reconstruction of an initial model, which was low-pass-filtered to 40  $\text{\AA}$  to use as the input reference map for 3D classification. Several rounds of 3D classification were used to produce homogeneous particle stacks among the heterogeneous particle populations (unbound DPP9, 2–2 and 2–4 DPP9–NLRP1 complexes). One selected 3D class (81,705 particles) was further 3D-refined. Subsequently, particles were symmetry-expanded (C2) and 3D-refined locally, followed by per-particle CTFRefine and Bayesian polishing to reach an overall resolution of 3.7  $\text{\AA}$  for the NLRP1–DPP9 complex. However, the map suffered from anisotropic resolution, and cryoEF<sup>35</sup> analysis estimated that data collected at a tilt angle of 37 $^\circ$  were ideal to fill the orientation gaps in Fourier space.

The overall processing scheme for the 37 $^\circ$  tilt data of the NLRP1–DPP9 complex was derived from a previously described workflow in Relion 3.0<sup>42</sup>. Template-free autopicking with crYOLO<sup>41</sup> picked 412,419 particles from the pre-processed micrographs. After several rounds of 2D classification, 378,410 visually homogenous particles remained for further processing. A random subset comprising 100,000 of these particles was used for de novo initial model construction, which was low-pass-filtered and used as the initial reference map for 3D classification. After several rounds of 3D classification, a 3D class with 89,601 particles remained. The first 3D refinement using these particles yielded an 8.9  $\text{\AA}$  resolution structure, and the Fourier shell correlation (FSC) curve showed strong fluctuations that indicated imprecisions in contrast-transfer function (CTF) estimation. To rectify this, we used CTF refinement and Bayesian polishing implemented in Relion 3.1, including higher-order aberration correction, anisotropic magnification correction and per-particle defocus estimation<sup>43</sup>. Iterative rounds of 3D refinement followed by CTF refinement and Bayesian polishing gradually improved the resolution and converged at a resolution plateau of 3.8  $\text{\AA}$ . Refined particle sets from 0 $^\circ$  and 37 $^\circ$  stage tilts were then merged and a final 3D refinement was performed. The merged data were reconstructed to an overall resolution of 3.6  $\text{\AA}$  with much improved FSC density. Gold-standard FSC between half maps are shown (Extended Data Fig. 1).

A similar data processing scheme was applied to 0° and 37° stage-tilted data of the NLRP1–DPP9–VbP complex. In brief, crYOLO-picked particles were 2D- and 3D-classified, leading to final sets composed of 118,113 and 124,781 particles at 0° and 37° stage tilts, respectively. Three-dimensional refinement followed by one iteration of CTF refinement and Bayesian polishing led to a 3.1 Å resolution map for the nontilt data. The 37°-stage-tilted particles initially resolved to 6.1 Å resolution, owing to inaccuracies in CTF estimation. To overcome this issue, particles were further refined; iterative 3D refinement followed by CTF refinement (higher-order aberration correction, anisotropic magnification correction and per-particle defocus estimation) gradually improved the resolution. Finally, tilted particles were subjected to Bayesian polishing followed by a final round of 3D refinement, which yielded a structure at 3.3 Å resolution. These two refined and polished particle sets (0° and 37° data) were then joined and refined, yielding a final map at 2.9 Å resolution calculated with the gold-standard FSC between half maps (Extended Data Fig. 4). Local resolution estimation for all maps was calculated with ResMap<sup>44</sup>.

### Atomic model building and structure representation

The cryo-EM maps were first fit with the crystal structure of DPP9 dimer (Protein Data Bank (PDB) code 6EQQ)<sup>24</sup>. A homology model of the FIIND of human NLRP1 (NLRP1(FIIND)) was generated with Schrodinger Prime<sup>45</sup> using the crystal structure of the rat NLRP1(FIIND) (PDB code 7CRV)<sup>46</sup> as a template. Initial model fitting in the map was performed with UCSF Chimera<sup>47</sup>. Manual adjustment and de novo building of missing segments, rigid-body fitting, flexible fitting and segment-based real-space refinement were performed in distinct parts of the initial model to fit in the density in Coot<sup>48</sup> and real-space refinement in Phenix<sup>49</sup>. A few unstructured regions, including parts of the UPA subdomain, were omitted owing to poor density. The full model represents residues D18–M1356 of DPP9, and ZU5 residues F1079–F1212, UPA<sup>A</sup> residues S1213–V1350 and UPA<sup>B</sup> residues S1213–M1356 of NLRP1.

For the VbP-bound structure, the full model represents residues D18–M1356 of DPP9, ZU5<sup>A</sup> residues F1079–F1212 and UPA<sup>A</sup> residues S1213–V1350. UPA<sup>B</sup> was not modelled owing to poor density. We modelled covalently linked DPP9(S730)–VbP in the cryo-EM map density based on the structure of the DPP9–VbP complex (PDB code 6HP8)<sup>50</sup> and independently validated fitting with the GemSpot pipeline<sup>51</sup>.

For both structures, interaction analysis was conducted visually and using PISA<sup>52</sup>. Structure representations were generated in UCSF ChimeraX<sup>53</sup> and Pymol<sup>54</sup>. Per residue C $\alpha$ –C $\alpha$  distances between the NLRP1-bound and VbP-bound DPP9 structures (Extended Data Fig. 5e) were calculated with the matchmaker function in UCSF Chimera<sup>47</sup> and the ColorByRMSD script in Pymol<sup>54</sup> script. Ligand interaction analysis was conducted with Maestro<sup>55</sup>. Pymol and ChimeraX session files are available from our Open Science Framework repository (<https://osf.io/x7dv8/>). Schematics were created with BioRender.

### CRISPR–Cas9 gene editing

Five hundred thousand *DPP9*-knockout HEK293T cells that stably express Cas9<sup>20</sup> were seeded in 6-well tissue culture dishes in 2 ml of medium per well. The next day, cells were transfected according to the manufacturer's instructions (FuGENE HD, Promega) with a mix of four single-guide RNA plasmids targeting *DPP9*. After 48 h of transfection, cells were transferred to a 10-cm tissue culture dish and selected with puromycin (2  $\mu\text{g ml}^{-1}$ ) until un-transfected control cells were dead. Single-cell clones were isolated by serial dilution and confirmed by genomic sequencing (Extended Data Fig. 7b).

### Immunoblotting

Samples were run on either NuPAGE 4 to 12%, Bis-Tris 1.0 mm, Mini Protein Gel (Invitrogen) for 30 min at 175 V or NuPAGE 4 to 12%, Bis-Tris, 1.0 mm, Midi Protein Gel (Invitrogen) for 45–60 min at 175 V. Gels were transferred to nitrocellulose with the Trans-Blot Turbo Transfer System

(BIO-RAD). Membranes were blocked with Intercept (TBS) Blocking Buffer (LI-COR) for 30 min at ambient temperature, before incubating with primary antibody overnight at 4 °C. Blots were washed 3 times with TBST buffer before incubating with secondary antibody for 60 min at ambient temperature. Blots were washed 3 times, rinsed with water and imaged via Odyssey CLx (LI-COR). Primary antibodies used in this study include: DPP9 rabbit polyclonal antibody (1:1,000, Abcam, Ab42080), Flag M2 mouse monoclonal antibody (1:1,000, Sigma, F3165), GAPDH rabbit monoclonal antibody (1:1,000, Cell Signaling Technology, 14C10), NLRP1 CT mouse monoclonal antibody (1:1,000, R&D Systems, MAB6788), CASP1 rabbit polyclonal antibody (1:1,000, Cell Signaling Technology, 2225), GSDMDC1 rabbit polyclonal antibody (1:1,000, Novus, NBP2-33422), V5 rabbit polyclonal antibody (1:1,000, Abcam, Ab9116) and HA-tag rabbit monoclonal antibody (1:1,000, Cell Signaling Technology, 3724). Secondary antibodies used in this study include: IRDye 680 RD streptavidin (1:1,000, LI-COR, 926-68079), IRDye 800CW anti-rabbit (1:10,000, LI-COR, 925-32211), IRDye 800CW anti-mouse (1:10,000, LI-COR, 925-32210), IRDye 680CW anti-rabbit (1:10,000, LI-COR, 925-68073) and IRDye 680CW anti-mouse (1:10,000, LI-COR, 925-68072).

### Immunoprecipitation assays

HEK293T cells were seeded at  $5 \times 10^5$  cells per well in 6-well tissue culture dishes. The following day, the cells were transfected with plasmids encoding the indicated Flag-tagged protein (2  $\mu\text{g}$ ) with FuGENE HD, according to manufacturer's instructions (Promega). After 48 h, cells were collected and washed 3 times with PBS. Pellets were lysed in Tris-buffered saline (TBS) with 0.5% NP-40 using pulse sonication and centrifuged at 20,000g for 10 min at 4 °C. Protein concentration of the soluble proteome was determined using the DC Protein Assay kit (Bio-Rad) and adjusted to 2 mg ml<sup>-1</sup>. Lysates were treated with DMSO or VbP (10  $\mu\text{M}$ ) for 1 h. Lysates were incubated with 20  $\mu\text{l}$  of anti-Flag–M2 agarose resin (Sigma) overnight at 4 °C. After washing  $3 \times 500 \mu\text{l}$  with cold PBS in microcentrifuge spin columns (Pierce), bound proteins were eluted by incubating resin with 40  $\mu\text{l}$  of PBS with 150 ng  $\mu\text{l}^{-1}$  3 $\times$ Flag peptide for 1 h at 4 °C. An equal volume of 2 $\times$  sample loading was added to the eluate and boiled. Immunoblots were developed with the Odyssey CLx imaging system (LI-COR).

For DPP9 mutants, *DPP8DPP9* double-knockout HEK293T cells were seeded at  $1 \times 10^6$  cells per well in 6-well tissue culture dishes. The following day, cells were transfected with plasmids encoding Flag-tagged NLRP1 (2  $\mu\text{g}$ ) or the indicated DPP9 construct (2  $\mu\text{g}$ ) with FuGENE HD, according to manufacturer's instructions (Promega). Cells were collected after 48 h, washed 3 times with PBS, lysed in Tris-buffered saline (TBS) with 0.5% NP-40 using pulse sonication and centrifuged at 20,000g for 10 min at 4 °C. Protein concentration of the soluble proteome was determined and normalized using the DC Protein Assay kit (Bio-Rad). Lysates were mixed in a one-to-one ratio of DPP9 and NLRP1 before treating with DMSO or VbP (10  $\mu\text{M}$ ) for 1 h. The assay was completed as described in the previous paragraph.

For on-bead displacement assay, HEK293T cells were seeded at  $3 \times 10^6$  cells in a 10-cm tissue culture dish. The following day, the cells were transfected with plasmids encoding Flag-tagged NLRP1(S1213A) (5  $\mu\text{g}$ ), V5-tagged DPP9 (3  $\mu\text{g}$ ) and MYC-tagged Ub–NLRP1 CT (2  $\mu\text{g}$ ) with FuGENE HD, according to manufacturer's instructions (Promega). Cells were collected and washed 3 $\times$  with PBS. Pellets were lysed in TBS with 0.5% NP-40 using pulse sonication and centrifuged at 20,000g for 10 min at 4 °C. Lysates were incubated with 100  $\mu\text{l}$  of anti-Flag–M2 agarose resin (Sigma) for 2 h at 4 °C. The agarose was washed once with PBS, and subsequently split into  $4 \times 25\text{-}\mu\text{l}$  aliquots, which were incubated with 50  $\mu\text{l}$  of PBS containing DMSO, VbP (10  $\mu\text{M}$ ), 8J (50  $\mu\text{M}$ ), bestatin methyl ester (10  $\mu\text{M}$ ) at room temperature for 1 h in microcentrifuge spin columns (Pierce). Displaced proteins were collected via centrifugation. The resin was washed 3 $\times$  with cold PBS, followed by elution with 40  $\mu\text{l}$  of PBS with 3 $\times$ Flag peptide. An equal volume of 2 $\times$  sample loading

## Article

was added to the eluate and boiled. Immunoblots were developed with the Odyssey CLx imaging system (LI-COR).

### DPP9 activity assay

A solution of substrate (1 mM Gly-Pro-AMC) was prepared in DMSO. Nineteen  $\mu\text{l}$  of PBS, recombinant DPP9 (1 nM) or the indicated cell lysate was added to a 384-well, black clear-bottom plate (Corning) followed by 1  $\mu\text{l}$  of substrate to initiate the reaction. Substrate cleavage was measured as increasing fluorescence signal recorded at ambient temperature every minute at 380-nm excitation and 460-nm emission wavelengths over a 30-min period. Activity was calculated by linear regression (Prism 7). For NLRP1 peptide assays, peptide or DMSO was added to the indicated final concentration and incubated for 30 min on ice before addition of Gly-Pro-AMC substrate.

### LDH cytotoxicity assay

HEK293T cells stably expressing CASP1 and GSDMD were seeded at  $1.25 \times 10^5$  cells per well in 12-well tissue culture dishes. The following day, the cells were transfected with plasmids encoding ASC (0.01  $\mu\text{g}$ ), the indicated NLRP1 construct (0.02  $\mu\text{g}$ ) and RFP (to 2  $\mu\text{g}$ ) (Fig. 3a, c, Extended Data Fig. 6g) or plasmids encoding ASC (0.01  $\mu\text{g}$ ), Ub-NLRP1 CT (0.02  $\mu\text{g}$ ), NLRP1(S1213A) (0.25, 1 and 2  $\mu\text{g}$ ) and RFP (to 2  $\mu\text{g}$ ) (Fig. 4c) with FuGENE HD (according to the manufacturer's instructions (Promega)) per 125  $\mu\text{l}$  of Opti-MEM. At 24 h, cells were treated with DMSO or VbP (10  $\mu\text{M}$ ). Twenty-four h later supernatants were analysed for LDH activity using the Pierce LDH Cytotoxicity Assay Kit (ThermoFisher) and lysate protein content was evaluated by immunoblotting. For NLRP1 CT experiments, LDH was measured and lysates were collected 24 h after transfection.

### dTAG-NLRP1 assay

HEK293T cells stably expressing CASP1 and GSDMD were seeded at  $1.25 \times 10^5$  cells per well in 12-well tissue culture dishes. The following day, the cells were transfected with plasmids encoding ASC (0.01  $\mu\text{g}$ ), dTAG-NLRP1 (0.025  $\mu\text{g}$ ), NLRP1(FIIND/S1213A) (indicated concentration) and RFP (to 1  $\mu\text{g}$ ) with FuGENE HD, according to the manufacturer's instructions (Promega). At 24 h, cells were treated with DMSO, dTAG13 (500 nM) and/or VbP (10  $\mu\text{M}$ ) for 6 h. Lysates were collected and protein content was evaluated by immunoblotting.

### ASC puncta formation assay

HEK293T cells were seeded at  $2.5 \times 10^5$  cells per ml in 12-well tissue culture dishes. The following day, the cells were transfected with plasmids encoding GFP-ASC (0.033  $\mu\text{g}$ ), the indicated NLRP1 construct (0.066  $\mu\text{g}$ ) and RFP (to 2  $\mu\text{g}$ ) (Fig. 3b, d, Extended Data Fig. 6h) or plasmids encoding GFP-ASC (0.02  $\mu\text{g}$ ), the indicated NLRP1 construct (0.05  $\mu\text{g}$ ), NLRP1(FIIND/S1213A) (0.5  $\mu\text{g}$ ) and RFP (to 2  $\mu\text{g}$ ) (Fig. 4d) with FuGENE HD (according to the manufacturer's instructions (Promega)) per 125  $\mu\text{l}$  of Opti-MEM. For the DPP9 experiment (Fig. 4g), *DPP8 DPP9* double-knockout HEK293T cells were seeded at  $2.5 \times 10^5$  cells per ml in 12-well tissue culture dishes and transfected the following day with plasmids encoding GFP-ASC (0.02  $\mu\text{g}$ ), NLRP1 (0.05  $\mu\text{g}$ ), NLRP1(FIIND/S1213A) (0.25  $\mu\text{g}$ ), the indicated DPP9 (0.5  $\mu\text{g}$ ) and RFP (to 2  $\mu\text{g}$ ) with FuGENE HD, according to the manufacturer's instructions (Promega), per 125  $\mu\text{l}$  of Opti-MEM. After 24 h, cells were treated with DMSO or VbP (10  $\mu\text{M}$ ) as indicated for 6 h. Nuclei were stained by treating cells with Hoechst dye (1  $\mu\text{l}$  of 1 mg  $\text{ml}^{-1}$  solution). Live-cell imaging was performed on a Zeiss Axio Observer.Z1 inverted wide-field microscope. For each chamber 5–15, positions were imaged on DAPI, and the red and green fluorescence channels at a single time point from a given experiment. Data were exported as raw .czi files and analysed using a custom macro written in ImageJ/FIJI. Total cell area was estimated from the RFP-positive signal, and the number of GFP-ASC specks was quantified using the 'Analyze particles' function following threshold adjustment in the GFP-positive images.

### dTAG ASC puncta formation assay

HEK293T cells were seeded at  $2.5 \times 10^5$  cells per ml in 12-well tissue culture dishes. The following day, the cells were transfected with constructs encoding GFP-ASC (0.02  $\mu\text{g}$ ), dTAG-NLRP1 (0.05  $\mu\text{g}$ ), NLRP1(FIIND/S1213A) (0.25 or 0.5  $\mu\text{g}$ ) and RFP (to 2  $\mu\text{g}$ ) with FuGENE HD, according to the manufacturer's instructions (Promega), per 125  $\mu\text{l}$  of Opti-MEM. After 24 h, cells were treated with DMSO or dTAG13 (500 nM) as indicated for 24 h. For the dTAG-NLRP1(P1214R) experiment (Fig. 4f), HEK293T cells were seeded at  $2.5 \times 10^5$  cells per ml in 12-well tissue culture dishes. The following day, the cells were transfected with constructs encoding GFP-ASC (0.02  $\mu\text{g}$ ), the indicated dTAG construct (0.05  $\mu\text{g}$ ), NLRP1(FIIND/S1213A) (0.5  $\mu\text{g}$ ) and RFP (to 2  $\mu\text{g}$ ) with FuGENE HD, according to the manufacturer's instructions (Promega), per 125  $\mu\text{l}$  of Opti-MEM. After 24 h cells, were treated with DMSO or dTAG13 (500 nM) as indicated for 16 h. Cells were imaged and quantified as described in 'ASC puncta formation assay'.

### Chemical enrichment of protease substrates

*DPP8 DPP9* double-knockout HEK293T cells were seeded at  $1 \times 10^6$  cells per well in 6-well tissue culture dishes. The following day, cells were transfected with plasmids encoding Flag-tagged NLRP1 (2  $\mu\text{g}$ ) with FuGENE HD, according to manufacturer's instructions (Promega). After 48 h, cells were collected, washed 3 $\times$  with PBS, lysed in PBS with pulse sonication and centrifuged at 20,000g for 10 min at 4  $^{\circ}\text{C}$ . Protein concentration of the soluble proteome was determined using the DC Protein Assay kit (Bio-Rad) and adjusted to 1.5 mg  $\text{ml}^{-1}$ .

Two hundred and fifty  $\mu\text{l}$  of lysate was incubated with PBS or recombinant DPP9 (about 3  $\mu\text{g}$ ). The activity of recombinant DPP9 was confirmed by Gly-Pro-AMC assay before its addition. The mixtures were allowed to incubate for 16 h at 37  $^{\circ}\text{C}$ , after which samples were boiled for 10 min to deactivate recombinant DPP9. A 2-pyridinecarboxaldehyde (2PCA)-biotin probe was added to lysates (10 mM final concentration) and incubated with shaking at 37  $^{\circ}\text{C}$  for an additional 16 h. Excess probe was removed by buffer exchange into fresh PBS with Amicon ultra 0.5-ml centrifugal filters, 10-kDa molecular mass cut-off (3  $\times$  500  $\mu\text{l}$ ). SDS was added to 1% and samples were boiled for 10 min, before diluting further with 5 ml of PBS. One hundred  $\mu\text{l}$  of high-capacity neutravidin agarose resin (Pierce) was added, before rotating tubes end-over-end for 1 h at room temperature. Samples were centrifuged at 1,000g for 2 min, supernatant was removed and beads were washed with 10 ml of PBS. This step was repeated a total of 3 times. Bound proteins were eluted by boiling the resulting neutravidin resin in 100  $\mu\text{l}$  of 2 $\times$  loading dye and evaluated by immunoblot.

### Reporting summary

Further information on research design is available in the Nature Research Reporting Summary linked to this paper.

### Data availability

Extended protein purification protocols are available on Protocols.io at <https://www.protocols.io/groups/hao-wu-lab>. Raw cryo-EM data are available on EMPIAR under the accession numbers EMPIAR-10594 (NLRP1-DPP9) and EMPIAR-10595 (NLRP1-DPP9-VbP). The cryo-EM maps are available on the Electron Microscopy Data Bank (EMDB) under the accession numbers EMD-22074 (NLRP1-DPP9) and EMD-22075 (NLRP1-DPP9-VbP). The atomic coordinates are available on the Protein Data Bank (PDB) under the accession numbers 6X6A (NLRP1-DPP9) and 6X6C (NLRP1-DPP9-VbP). Pymol session files and the image analysis macro are available from <https://doi.org/10.17605/OSF.IO/X7DV8>. All other data can be obtained from the corresponding authors upon reasonable request. Source data are provided with this paper.

32. Johnson, D. C. et al. DPP8/DPP9 inhibitor-induced pyroptosis for treatment of acute myeloid leukemia. *Nat. Med.* **24**, 1151–1156 (2018).
33. Mintseris, J. & Gygi, S. P. High-density chemical cross-linking for modeling protein interactions. *Proc. Natl Acad. Sci. USA* **117**, 93–102 (2020).
34. Mastrorade, D. N. Automated electron microscope tomography using robust prediction of specimen movements. *J. Struct. Biol.* **152**, 36–51 (2005).
35. Naydenova, K. & Russo, C. J. Measuring the effects of particle orientation to improve the efficiency of electron cryomicroscopy. *Nat. Commun.* **8**, 629 (2017).
36. Morin, A. et al. Collaboration gets the most out of software. *eLife* **2**, e01456 (2013).
37. Towns, J. et al. XSEDE: accelerating scientific discovery. *Comput. Sci. Eng.* **16**, 62–74 (2014).
38. Zheng, S. Q. et al. MotionCor2: anisotropic correction of beam-induced motion for improved cryo-electron microscopy. *Nat. Methods* **14**, 331–332 (2017).
39. Rohou, A. & Grigorieff, N. CTFIND4: fast and accurate defocus estimation from electron micrographs. *J. Struct. Biol.* **192**, 216–221 (2015).
40. Su, M. goCTF: geometrically optimized CTF determination for single-particle cryo-EM. *J. Struct. Biol.* **205**, 22–29 (2019).
41. Wagner, T. et al. SPHIRE-cryoLO is a fast and accurate fully automated particle picker for cryo-EM. *Commun. Biol.* **2**, 218 (2019).
42. Zivanov, J. et al. New tools for automated high-resolution cryo-EM structure determination in RELION-3. *eLife* **7**, e42166 (2018).
43. Zivanov, J., Nakane, T. & Scheres, S. H. W. Estimation of high-order aberrations and anisotropic magnification from cryo-EM data sets in RELION-3.1. *IUCr J*, 253–267 (2020).
44. Kucukelbir, A., Sigworth, F. J. & Tagare, H. D. Quantifying the local resolution of cryo-EM density maps. *Nat. Methods* **11**, 63–65 (2014).
45. Jacobson, M. P., Friesner, R. A., Xiang, Z. & Honig, B. On the role of the crystal environment in determining protein side-chain conformations. *J. Mol. Biol.* **320**, 597–608 (2002).
46. Huang, M. et al. Structural and biochemical mechanisms of NLRP1 inhibition by DPP9. *Nature* <https://doi.org/10.1038/s41586-021-03320-w> (2021).
47. Goddard, T. D., Huang, C. C. & Ferrin, T. E. Visualizing density maps with UCSF Chimera. *J. Struct. Biol.* **157**, 281–287 (2007).
48. Emsley, P., Lohkamp, B., Scott, W. G. & Cowtan, K. Features and development of Coot. *Acta Crystallogr. D* **66**, 486–501 (2010).
49. Klaholz, B. P. Deriving and refining atomic models in crystallography and cryo-EM: the latest Phenix tools to facilitate structure analysis. *Acta Crystallogr. D* **75**, 878–881 (2019).
50. Diaz, B. H. R. *Improvement of Protein Crystal Diffraction Using Post-Crystallization Methods: Infrared Laser Radiation Controls Crystal Order*. PhD thesis, Universität Hamburg (2018).
51. Robertson, M. J., van Zundert, G. C. P., Borrelli, K. & Skiniotis, G. GemSpot: a pipeline for robust modeling of ligands into cryo-EM maps. *Structure* **28**, 707–716.e3 (2020).
52. Krissinel, E. & Henrick, K. Inference of macromolecular assemblies from crystalline state. *J. Mol. Biol.* **372**, 774–797 (2007).
53. Goddard, T. D. et al. UCSF ChimeraX: Meeting modern challenges in visualization and analysis. *Protein Sci.* **27**, 14–25 (2018).
54. Schrödinger. The PyMOL Molecular Graphics System, version 2.0, <https://pymol.org/2/> (2020).
55. Schrödinger. Maestro, release 2020-4, <https://www.schrodinger.com/products/maestro> (2020).

**Acknowledgements** We thank T.-m. Fu of the laboratory of H.W. for initiating an apo-NLRP1 project; all members of the laboratories of H.W. and D.A.B. for helpful discussions; J. Chai for sharing their crystal structure of the FIIND of rat NLRP1 before submission; M. Su for his advice on running goCTF and CTF estimation for tilt datasets; M. Ericsson at the HMS electron microscopy facility for advice and training; R. Walsh, S. Sterling and S. Rawson at the Harvard Cryo-EM Center for Structural Biology for cryo-EM training and productive consultation; G. Skiniotis and M. Robertson for sharing their GemSpot script and for troubleshooting advice; T. Edwards and the National Cancer Institute's National Cryo-EM Facility at the Frederick National Laboratory for Cancer Research under contract HSSN261200800001E; and J. Myers and the Pacific Northwest Center for Cryo-EM at Oregon Health & Science University for screening and preliminary dataset collection, under the NIH grant U24GM129547 and accessed through EMSL (grid.436923.9), a DOE Office of Science User Facility sponsored by the Office of Biological and Environmental Research. The pcDNA3.1 LIC 6A and pcDNA 3.1 LIC 6D plasmids were gifts from S. Gradia (Addgene plasmids no. 30124 and no. 30127, respectively). The pLEX\_305-N-dTAG plasmid was a gift from J. Bradner and B. Nabet (Addgene plasmid no. 91797). The pLEX\_307 plasmid was a gift from D. Root (Addgene plasmid no. 41392). Our research used software and computing support at SBGrid and the Extreme Science and Engineering Discovery Environment (XSEDE) Bridges at the Pittsburgh Supercomputing Center, through allocation TG-MCB190086. This work was supported by the National Institutes of Health and the Cancer Research Institute (DP1 HD087988 and R01 AI124491 to H.W., T32-GM007726 to L.R.H., the CRI Irvington Postdoctoral Fellowship to P.F., R01GM132129 to J.A.P., R01GM67945 to S.P.G., T32 GM007739-Andersen and F30 CA243444 to A.R.G. and the Memorial Sloan Kettering Cancer Center Core Grant P30 CA008748 and R01 AI137168 to D.A.B.). We apologize to authors whose work could not be cited because of space limitation.

**Author contributions** L.R.H., H.S. and H.W. conceived the NLRP1–DPP9 complex study. L.R.H. designed constructs with input from H.S. L.R.H., H.S., P.F. and K.B.D. carried out preliminary expression and purification studies. L.R.H. purified the complexes. H.S. and L.R.H. made cryo-EM grids for data collection. L.R.H. screened cryo-EM grids and collected cryo-EM data. H.S. and L.R.H. analysed cryo-EM data. H.S. performed model building and refinement. L.R.H. and H.S. designed mutants for in vitro and cell-based assays. L.R.H. and A.R.G. cloned mutants for functional study. A.R.G. performed all cell-based assays, peptide mass spectrometry and chemical enrichment of protease substrates analysis under the supervision of D.A.B. J.M. and J.A.P. performed crosslinking mass spectrometry and data analysis under the supervision of S.P.G. A.R.G., L.R.H., H.S., H.W. and D.A.B. designed the experiments. L.R.H., H.S., A.R.G., H.W. and D.A.B. wrote the manuscript with input from all of the other authors.

**Competing interests** H.W. is a co-founder of Ventus Therapeutics. The other authors declare no competing interests.

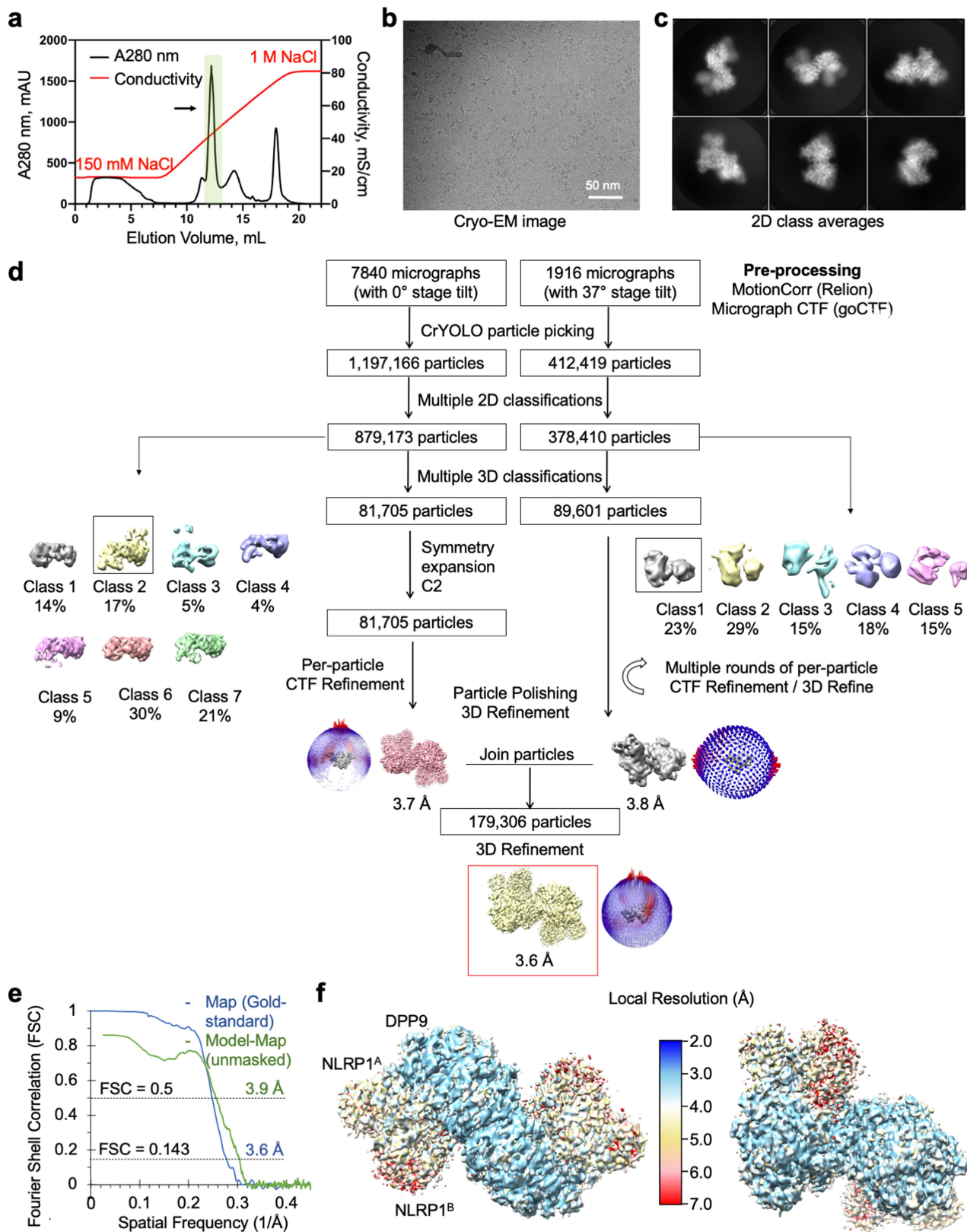
#### Additional information

**Supplementary information** The online version contains supplementary material available at <https://doi.org/10.1038/s41586-021-03350-4>.

**Correspondence and requests for materials** should be addressed to D.A.B. or H.W.

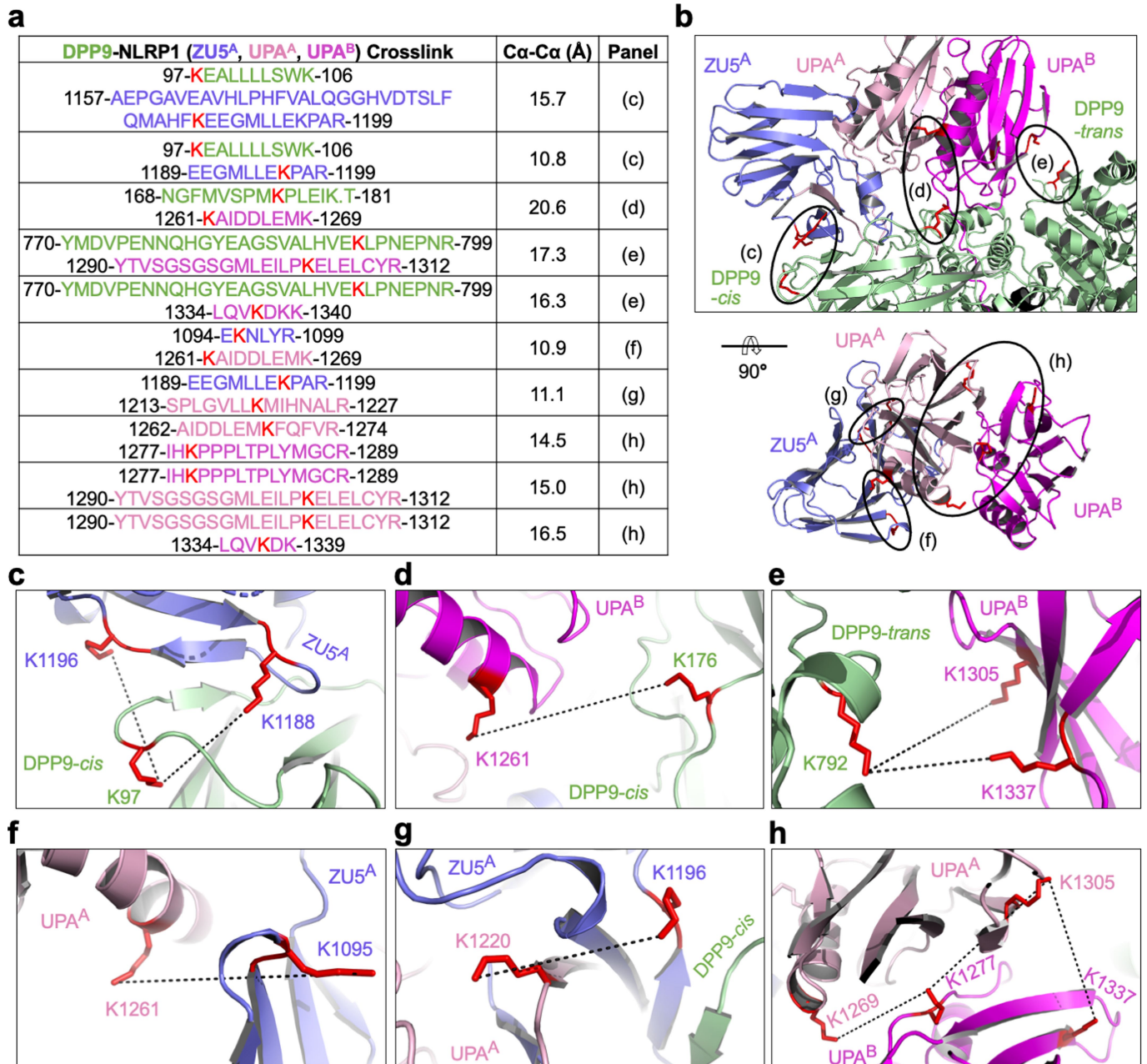
**Peer review information** Nature thanks Edward Miao and the other, anonymous, reviewer(s) for their contribution to the peer review of this work.

**Reprints and permissions information** is available at <http://www.nature.com/reprints>.



**Extended Data Fig. 1 | Structural determination of the NLRP1-DPP9 complex.** **a**, Purification of the NLRP1-DPP9 complex by ion-exchange chromatography. The ternary complex peak is shaded in green and labelled with an arrow. **b**, A representative (of >1,000 images) cryo-EM micrograph.

**c**, Representative 2D class averages. **d**, Workflow for the determination of the structure of the NLRP1-DPP9 complex. **e**, Map-map and map-model FSC curves. **f**, Local-resolution distribution of the final map calculated with ResMap<sup>44</sup>.



**Extended Data Fig. 2 | Crosslinking mass spectrometry analysis of the NLRP1-DPP9 complex.** **a**, Summary of BS3 crosslinking between DPP9 and NLRP1. High-confidence crosslinked peptides are displayed, and residue ranges are labelled and colour-coded by domain. Crosslinked lysine pairs are indicated in red text. Ca-Ca distances between lysine residues (in red)

interpreted by the final NLRP1-DPP9 model are shown, along with the figure panels that show them in detail. All detected peptide pairs are tabulated in Source Data. **b**, Overview of BS3-mediated crosslinks. **c-h**, Close-up views highlighting crosslinked lysine pairs (red) interpreted by the final NLRP1-DPP9 model.



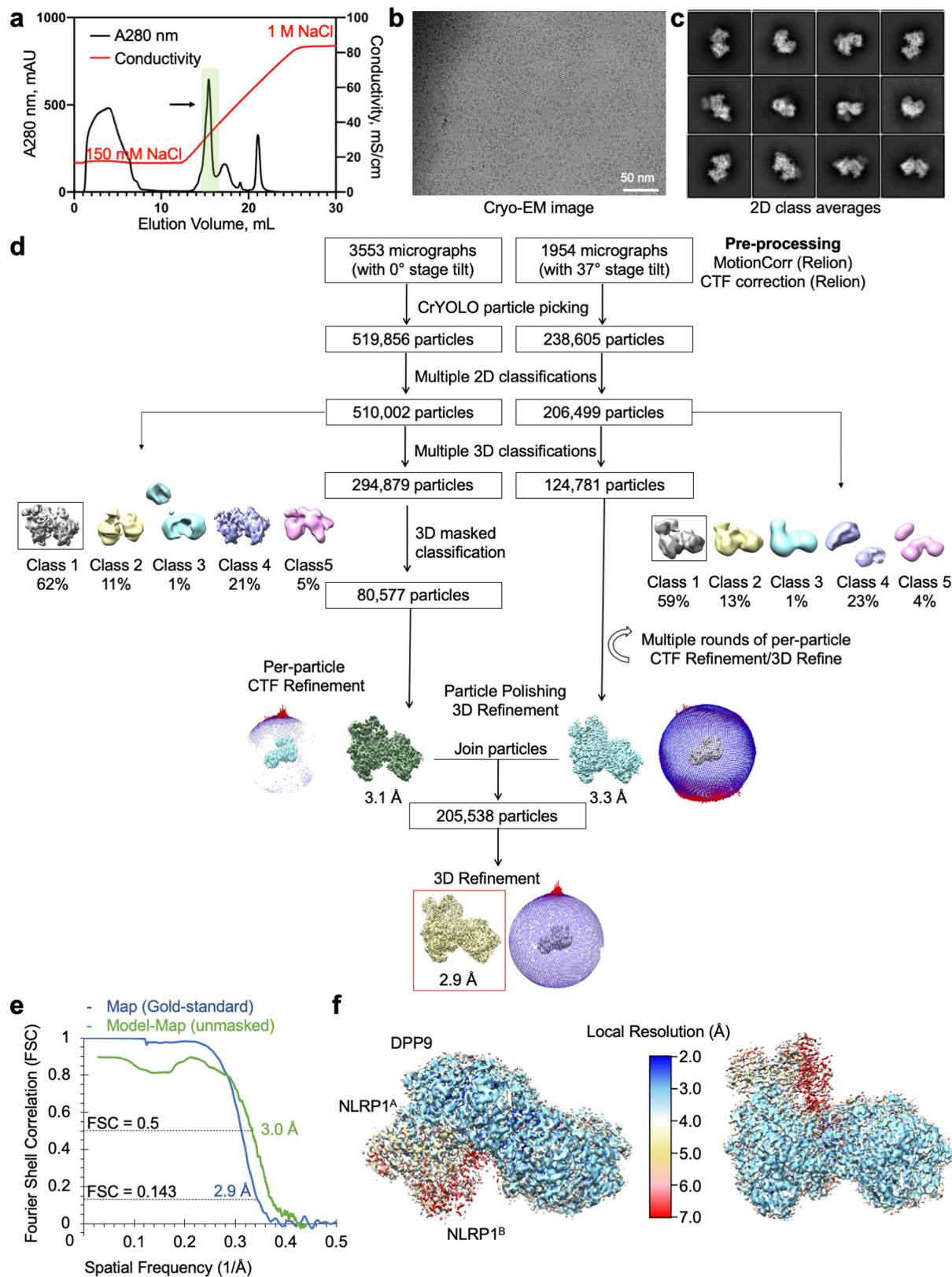
**Extended Data Fig. 3 | Sequence and structural analysis of FIIND.**

**a**, ClustalW multiple sequence alignment between human NLRP1 (hNLRP1), mouse NLRP1 (mNLRP1, different isoforms) and rat NLRP1 (rNLRP1, different isoforms). COP, Copenhagen; ZUC, Zucker; LEW, Lewis; SD, Sprague Dawley; and CDF, Fischer. Secondary structures and residue numbers are denoted on the basis of the human FIIND<sup>A</sup> structure in the NLRP1–DPP9 ternary complex. Interface residues in the NLRP1–DPP9 complex are annotated with asterisks, and residues in the catalytic triad (H1186, E1195 and S1213) are boxed in black. **b**, FIIND<sup>A</sup> overview with ZU5 (blue) and UPA (light pink) subdomains. The

catalytic triad residues (H1186, E1195 and S1213) are shown in sticks.

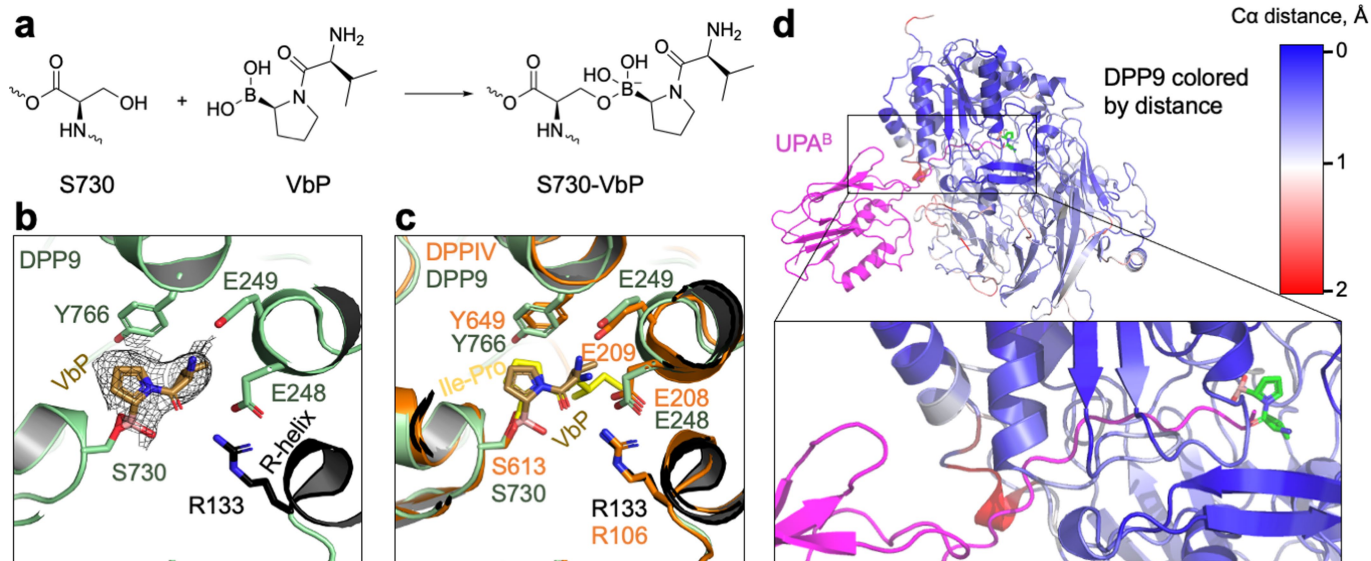
**c**, Topology of the FIIND with secondary structures labelled.

**d**, Superimposition of FIIND<sup>A</sup> onto the UPA<sup>B</sup>. NLRP1<sup>B</sup> must be free NLRP1 CT, because a ZU5 subdomain at site B would have clashed with ZU5 and UPA at site A and with DPP9. **e**, The ZU5<sup>A</sup>–UPA<sup>A</sup>–UPA<sup>B</sup> module that binds DPP9. UPA<sup>A</sup> and UPA<sup>B</sup> interact with each other in a front-to-back manner, with only a 9° rotation between them. **f**, Altered conformation of the UPA<sup>B</sup> N terminus that binds in the DPP9 active-site tunnel in comparison to UPA<sup>A</sup> in a complete FIIND<sup>A</sup>.



**Extended Data Fig. 4 | Structural determination of the NLRP1-DPP9 complex with VbP.** **a**, Purification of the NLRP1-DPP9 complex in the presence of VbP by ion-exchange chromatography. The ternary complex peak is shaded in green and labelled with an arrow. **b**, A representative (of >1,000 images)

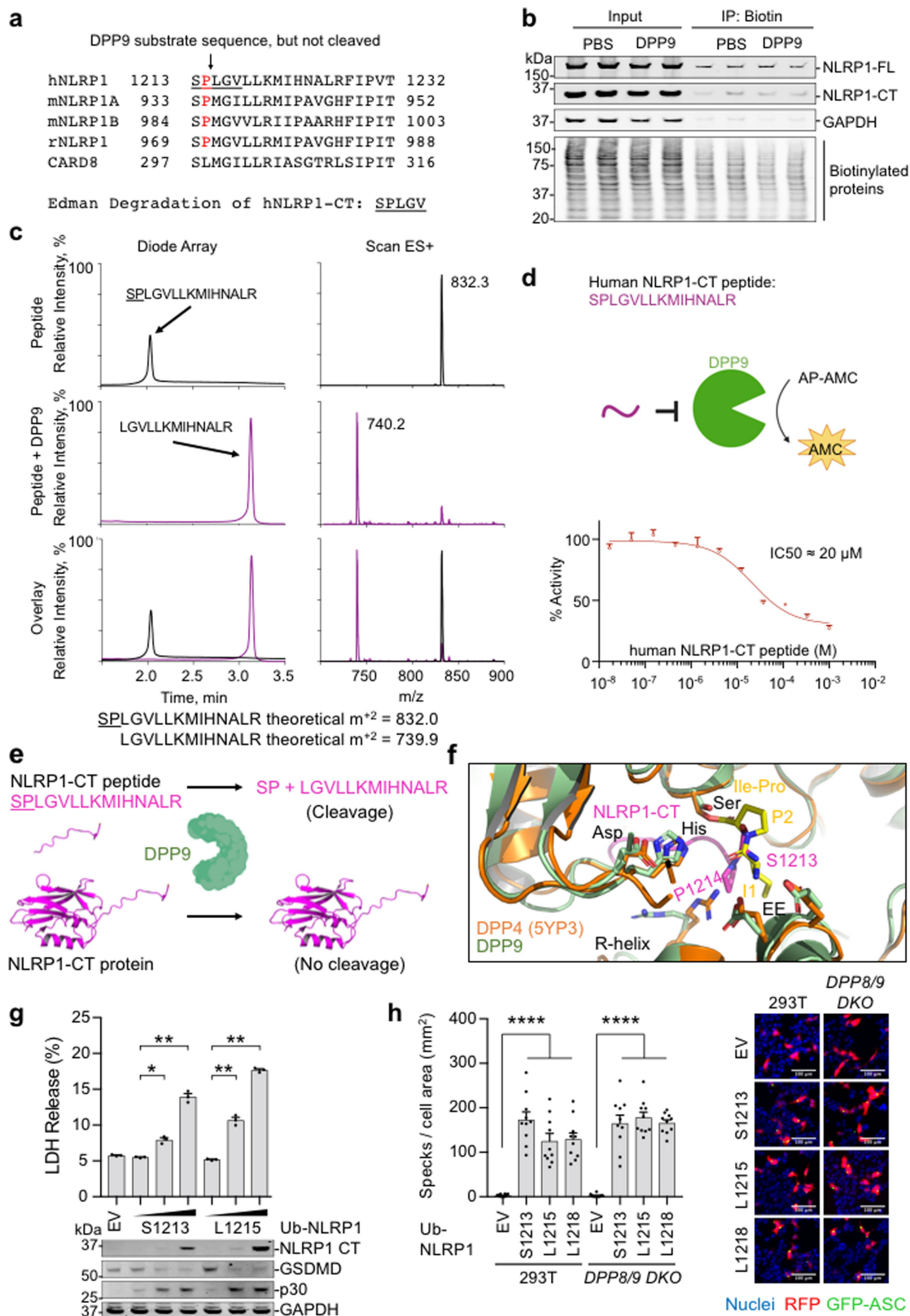
cryo-EM micrograph. **c**, Representative 2D class averages. **d**, Workflow for the determination of the structure of the NLRP1-DPP9-VbP complex. **e**, Map-map and map-model FSC curves. **f**, Local-resolution distribution of the final map calculated with ResMap<sup>44</sup>.



**Extended Data Fig. 5 | VbP interactions in the DPP9 active site and**

**comparison to a DPP substrate and NLRP1.** **a**, Schematic of covalent linkage between the S730 of DPP9 and VbP. **b**, Fit of VbP into the cryo-EM density. VbP is shown in stick, with carbon atoms in light brown. The charged amino group of VbP interacts with the DPP9 EE-loop (which also coordinates a substrate N terminus), and the carbonyl oxygen of VbP interacts with R133 of the R helix. The covalent linkage of VbP with S730 (the catalytic serine) is displayed. **c**, Structural alignment of the VbP-bound DPP9 model (green) and the crystal

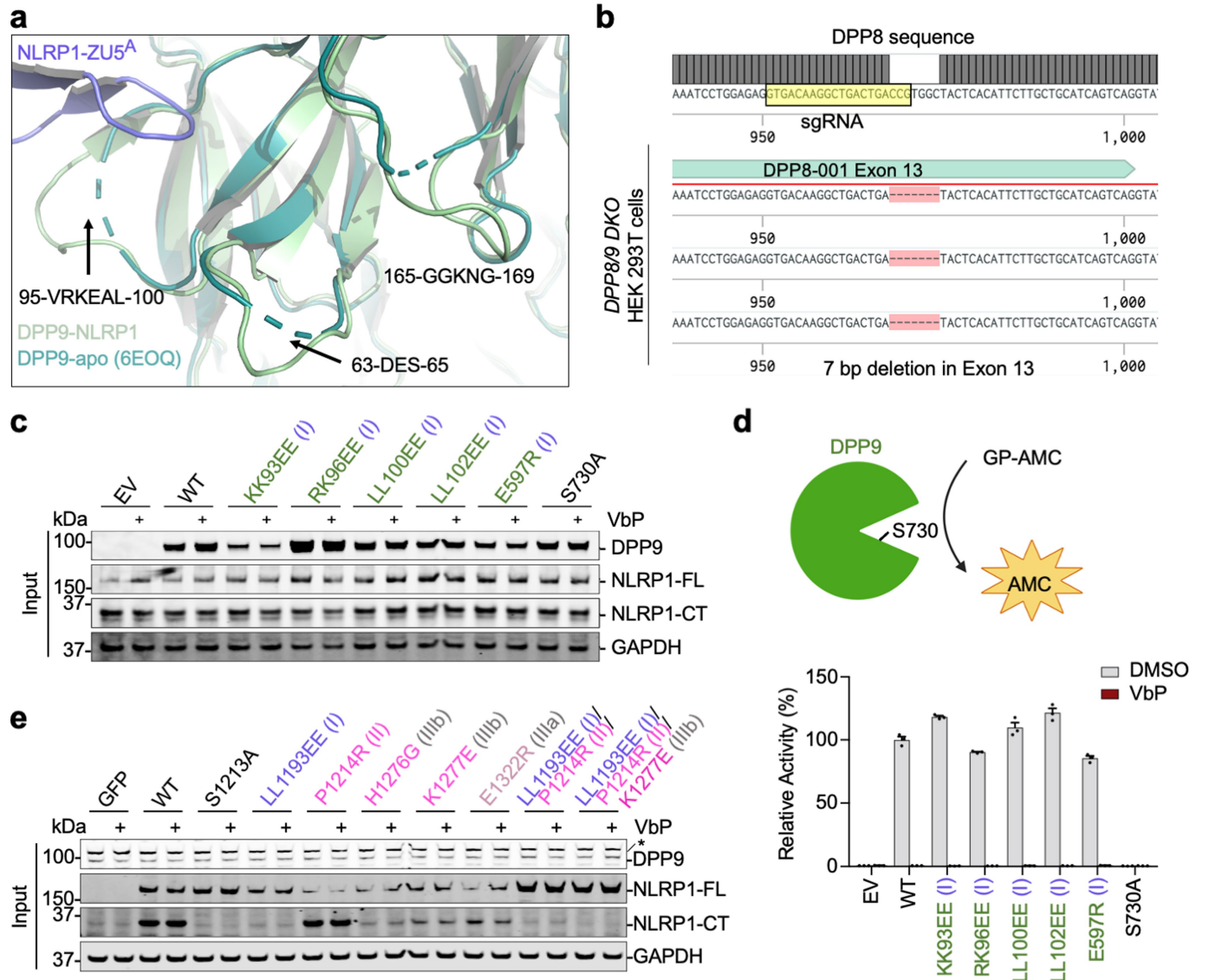
structure of bacterial DPP4 bound to the substrate Ile-Pro (PDB code 5YP3) (orange)<sup>25</sup>. VbP assumes a pose that is notable similar to a model substrate. **d**, NLRP1 CT-DPP9 complex, in which DPP9 is coloured by Ca-Ca distances between NLRP1-bound and VbP-bound structures, as indicated. A distance scale bar is shown. VbP is displayed in sticks to mark the active site, with carbon atoms in green, oxygen atoms in red, nitrogen atoms in blue and boron atoms in orange. UPA of NLRP1 CT is shown in magenta.



Extended Data Fig. 6 | See next page for caption.

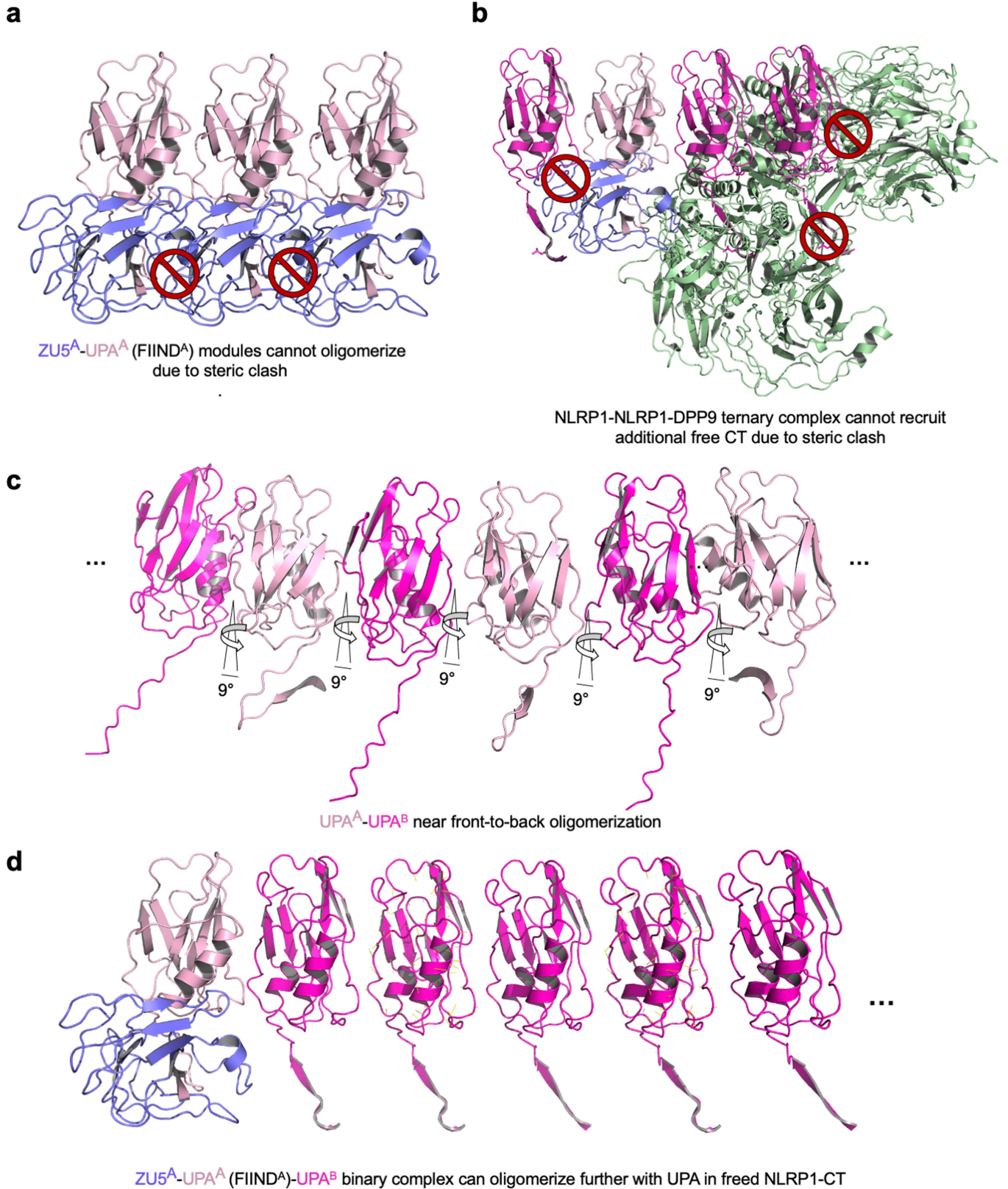
**Extended Data Fig. 6 | Lack of cleavage of intact NLRP1CT, but the cleavage of its isolated N-terminal peptide, by DPP9.** **a**, N-terminal sequencing of the purified NLRP1–DPP9 complex, showing that the NLRP1CT is not cleaved by the co-expressed DPP9. **b**, Chemical enrichment of protease substrates assay, showing that DPP9 does not cleave NLRP1CT. In brief, wild-type NLRP1 expressed in *DPP8DPP9* double-knockout HEK293T cells was incubated with PBS or recombinant DPP9 before labelling with a 2PCA–biotin probe (which selectively biotinylates free N termini, except for those with a proline in the second position), followed by capture of biotinylated proteins. The inputs and the eluents were analysed by immunoblots using anti-NLRP1CT (full-length NLRP1 and NLRP1CT), anti-GAPDH and anti-streptavidin (biotinylated proteins) antibodies. DPP9 treatment did not increase the biotinylation of NLRP1CT, as would be expected after the removal of the N-terminal Ser-Pro dipeptide. **c**, Evidence of cleavage of the isolated 15-residue N-terminal peptide in NLRP1CT by recombinant DPP9 from mass spectrometry analysis. **d**, Inhibition of DPP9 catalytic activity against Ala-Pro-AMC by the isolated

NLRP1CT peptide. **e**, Schematic illustrates the ability of DPP9 to cleave an isolated UPA N-terminal peptide, but not dipeptides from an intact NLRP1CT. **f**, Comparison of the binding modes of the UPA<sup>B</sup> N-terminal peptide in the NLRP1–DPP9 complex and the Ile-Pro dipeptide in an acyl-enzyme intermediate<sup>25</sup>. **g**, Theoretical dipeptide cleavage does not dampen activity of the NLRP1 inflammasome by LDH release or inflammasome signalling.  $n = 3$  independent biological replicates. Data are mean  $\pm$  s.e.m. Anti-Flag (NLRP1CT), anti-GSDMD and anti-GAPDH antibodies were used in the immunoblots. p30, GSDMD N-terminal fragment from caspase-1 cleavage. **h**, Theoretical dipeptide cleavage does not dampen activity of the NLRP1 inflammasome by formation of ASC specks.  $n = 10$  quantified fields of view. Data are mean  $\pm$  s.e.m. Right, representative superimposed images of nuclei (blue), RFP (red) and GFP–ASC (green). All data are representative of  $>2$  independent experiments. \* $P < 0.05$ , \*\* $P < 0.01$ , \*\*\* $P < 0.001$ , \*\*\*\* $P < 0.0001$  by unpaired two-sided *t*-test. Exact *P* values are provided in Source Data.



**Extended Data Fig. 7 | Mutational analysis of the interactions in the NLRP1-DPP9 ternary complex.** **a**, Disorder-to-order transition of several DPP9 surface loops from the isolated DPP9 crystal structure (PDB code 6EOQ)<sup>24</sup> to the NLRP1-bound DPP9 cryo-EM structure. **b**, Genomic confirmation of DPP8 knockout generated in *DPP9*-knockout HEK293T cells that stably express Cas9<sup>20</sup>, to create *DPP8DPP9* double-knockout HEK293T cells. The single-guide RNA (sgRNA) sequence is highlighted. **c**, Immunoblots of the input lysates for the Flag co-immunoprecipitation with wild-type or mutant DPP9 and wild-type NLRP1-Flag, related to Fig. 2h. Anti-DPP9, anti-NLRP1 (full-length NLRP1 and

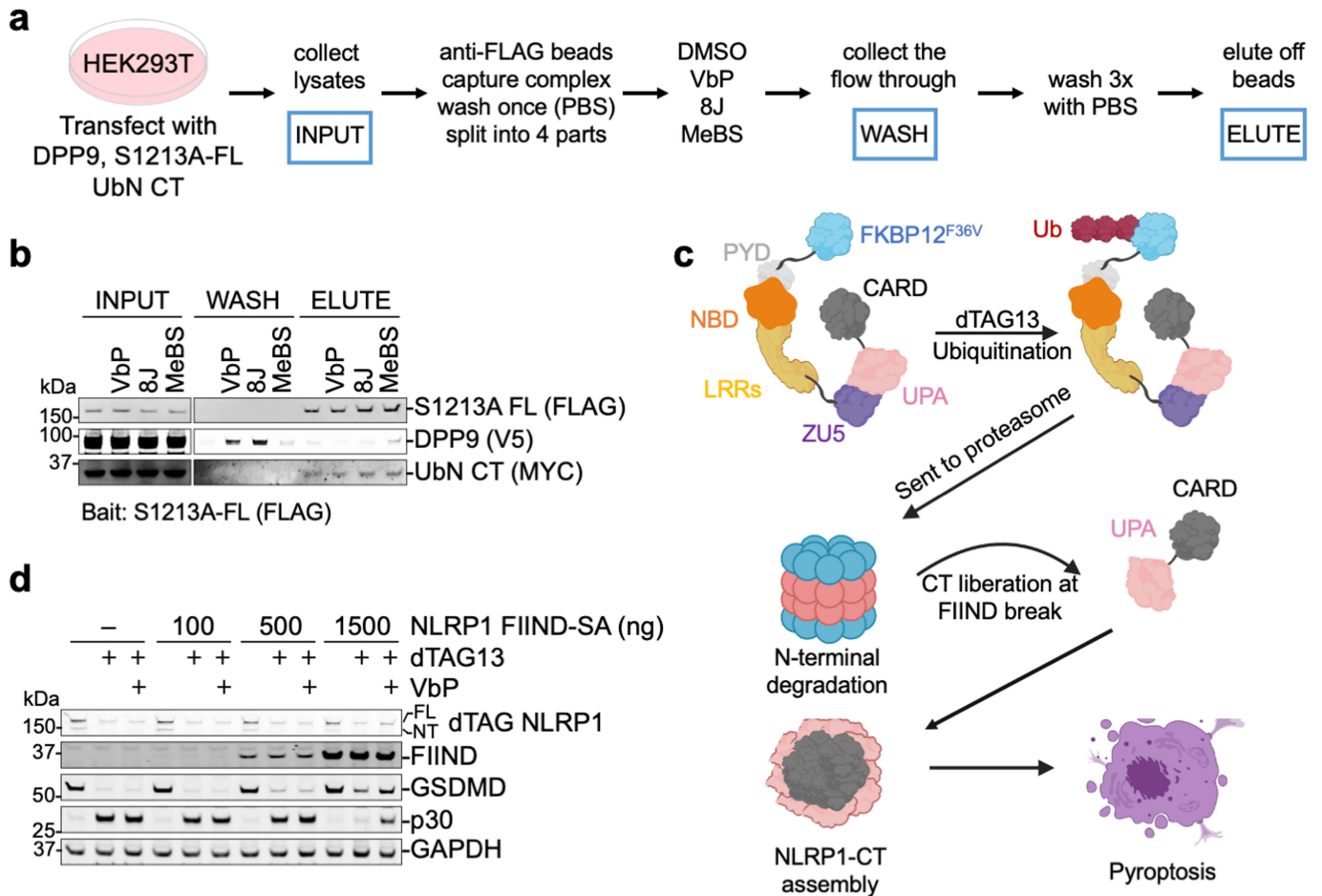
NLRP1 CT) and anti-GAPDH antibodies were used in the immunoblots. **d**, Cleavage rate of a model DPP9 substrate, Gly-Pro-AMC, by wild-type DPP9 and its structure-guided mutants. Only the catalytically dead mutant DPP9(S730A) disrupts catalytic activity and sensitivity to VbP. *n* = 3 technical replicates. Data are mean ± s.e.m. **e**, Immunoblots of the input lysates for the Flag co-immunoprecipitation with wild-type or mutant NLRP1-Flag and wild-type DPP9, related to Fig. 2i. Anti-DPP9, anti-NLRP1 (full-length NLRP1 and NLRP1 CT) and anti-GAPDH antibodies were used in the immunoblots. All data are representative of >2 independent experiments.



**Extended Data Fig. 8 | The ZU5 domain and DPP9 sterically hinder UPA polymerization. a**, Modelling of a FIIND polymer using the observed UPA<sup>A</sup>-UPA<sup>B</sup> relationship. Adjacent ZU5 molecules would clash, which suggests that UPA polymerization cannot occur in complete FIIND. **b**, Modelled recruitment of free UPA adjacent to UPA<sup>A</sup> and UPA<sup>B</sup> in the ternary complex with DPP9. The additional UPA subdomain next to FIIND<sup>A</sup> clashes with the ZU5 subdomain, and the additional UPA next to UPA<sup>B</sup> clashes with both DPP9 monomers in the complex, which suggests that DPP9 inhibits UPA oligomerization. **c**, A

modelled UPA oligomer on the basis of the near front-to-back interaction in the NLRP1-DPP9 ternary complex. In the model, the N-terminal tails of free UPAs are shown in the UPA<sup>A</sup> (pink) or UPA<sup>B</sup> (magenta) conformation in complex with DPP9 but, in reality, this conformation is likely to be different. **d**, Modelling of a UPA oligomer formed on one side of a NLRP1 FIIND<sup>A</sup>-NLRP1 CT<sup>B</sup> complex. The NLRP1 FIIND<sup>A</sup>-NLRP1 CT<sup>B</sup> binary complex can polymerize with freed NLRP1 CT. In **a-d**, DPP9 is coloured in green, and NLRP1 domains are coloured as indicated.

# Article



## Extended Data Fig. 9 | VbP displaces NLRP1 from DPP9 in vitro and in cells.

**a**, Schematic of the on-bead displacement experiment. The ternary complex is expressed in HEK293T cells, which are then lysed and incubated with Flag beads. Once bound, beads are split equally and washed with compounds or DMSO. The remainder of the protein is eluted off of the beads. MeBS, bestatin methyl ester. **b**, Two structurally distinct DPP9 inhibitors (VbP and 8J) displace DPP9 from NLRP1(S1213A) by the on-bead displacement assay. Anti-Flag (NLRP1(S1213A)), anti-MYC (NLRP1 CT) and anti-V5 (DPP9) antibodies were used in the immunoblots. Representative of two independent experiments. **c**, Schematic of the dTAG experiment. FKBP12 with the F36V mutation (dTAG) is fused to the N terminus of NLRP1. The dTAG13 ligand recruits an E3 ligase to

FKBP12(F36V), leading to its ubiquitination and N-terminal degradation of the fusion protein. NLRP1 CT (UPA-CARD) that results from FIIND autoprocessing are released to assemble the inflammasome. **d**, NLRP1(FIIND/S1213A) expression in reconstituted HEK293T inflammasome system rescues GSDMD cleavage resulting from dTAG13-induced NLRP1 degradation. VbP prevents GSDMD rescue without inducing additional NLRP1 degradation. Anti-HA (dTAG-NLRP1, and dTAG-NLRP1 N-terminal fragment), anti-Flag (NLRP1(FIIND/S1213A)), anti-GSDMD and anti-GAPDH antibodies were used in the immunoblots. p30, GSDMD N-terminal fragment from caspase-1 cleavage. Representative of two independent experiments.

**Extended Data Table 1 | Cryo-EM data collection and refinement statistics of NLRP1-DPP9 structures**

	NLRP1-DPP9		NLRP1-DPP9-VbP	
Stage tilt (°)	0°	37°	0°	37°
Movies collected	7,840	1,916	3,553	1,954
Magnification	105,000	105,000	105,000	105,000
Voltage (kV)	300	300	300	300
Electron exposure (e <sup>-</sup> /Å <sup>2</sup> )	67.54	67.6	52	65
Defocus range (μm)	-1.0 to -2.5	-1.5 to -3.0	-0.8 to -2.2	-1.5 to -3.0
Exposure time (s)	1.8	2.6	2.0	2.4
Pixel size (Å)	0.825	0.825	0.825	0.825
Symmetry imposed	C1	C1	C1	C1
Initial particle images (no.)	758,461	398,698	1,1609,585	239,416
	Merged Data		Merged Data	
Final particle images (no.)	179,306		205,538	
Map resolution (Å)	3.6		2.9	
FSC threshold	0.143		0.143	
<b>Refinement</b>				
Model resolution (Å)	3.9		2.9	
FSC threshold	0.5		0.5	
Map sharpening <i>B</i> factor (Å <sup>2</sup> )	-81.4		-49.0	
<b>Model composition</b>				
Non-hydrogen atoms	20,269		15,806	
Protein residues	2,524		1964	
Ligands			2	
B factors (Å <sup>2</sup> )	110.1		82.7	
<b>R.m.s. deviations</b>				
Bond lengths (Å)	0.011		0.008	
Bond angles (°)	1.327		1.363	
<b>Validation</b>				
MolProbity score	1.93		1.88	
Clashscore	8.55		7.21	
Poor rotamers (%)	0.00		0.00	
<b>Ramachandran plot</b>				
Favoured (%)	92.1		93.3	
Allowed (%)	7.7		6.5	
Disallowed (%)	0.1		0.2	

## Reporting Summary

Nature Research wishes to improve the reproducibility of the work that we publish. This form provides structure for consistency and transparency in reporting. For further information on Nature Research policies, see our [Editorial Policies](#) and the [Editorial Policy Checklist](#).

### Statistics

For all statistical analyses, confirm that the following items are present in the figure legend, table legend, main text, or Methods section.

- | n/a                                 | Confirmed  |
|-------------------------------------|--|
| <input type="checkbox"/>            | <input checked="" type="checkbox"/> The exact sample size ( $n$ ) for each experimental group/condition, given as a discrete number and unit of measurement  |
| <input type="checkbox"/>            | <input checked="" type="checkbox"/> A statement on whether measurements were taken from distinct samples or whether the same sample was measured repeatedly  |
| <input type="checkbox"/>            | <input checked="" type="checkbox"/> The statistical test(s) used AND whether they are one- or two-sided<br><i>Only common tests should be described solely by name; describe more complex techniques in the Methods section.</i>   |
| <input type="checkbox"/>            | <input checked="" type="checkbox"/> A description of all covariates tested   |
| <input type="checkbox"/>            | <input checked="" type="checkbox"/> A description of any assumptions or corrections, such as tests of normality and adjustment for multiple comparisons  |
| <input type="checkbox"/>            | <input checked="" type="checkbox"/> A full description of the statistical parameters including central tendency (e.g. means) or other basic estimates (e.g. regression coefficient) AND variation (e.g. standard deviation) or associated estimates of uncertainty (e.g. confidence intervals) |
| <input type="checkbox"/>            | <input checked="" type="checkbox"/> For null hypothesis testing, the test statistic (e.g. $F$ , $t$ , $r$ ) with confidence intervals, effect sizes, degrees of freedom and $P$ value noted<br><i>Give <math>P</math> values as exact values whenever suitable.</i>                            |
| <input checked="" type="checkbox"/> | <input type="checkbox"/> For Bayesian analysis, information on the choice of priors and Markov chain Monte Carlo settings  |
| <input checked="" type="checkbox"/> | <input type="checkbox"/> For hierarchical and complex designs, identification of the appropriate level for tests and full reporting of outcomes  |
| <input checked="" type="checkbox"/> | <input type="checkbox"/> Estimates of effect sizes (e.g. Cohen's $d$ , Pearson's $r$ ), indicating how they were calculated  |

*Our web collection on [statistics for biologists](#) contains articles on many of the points above.*

### Software and code

Policy information about [availability of computer code](#)

Data collection We used SerialEM v3.8.0 Beta for automated collection of cryo-EM data.

Data analysis MotionCor2, CTFFIND4.1.13, goCTF v1.2.0, crYOLO v1.3.6 and v1.5.3, RELION3.08, RELION3.1, ResMAP v1.1.4, Coot v0.8.9.1, Phenix v1.18.2-3874, pymol v2.4.0, chimera v1.14, chimeraX v1.0, Schrodinger prime 2020-1, PIXL search engine v1.0, ImageJ v2.0, GraphPad PRISM 7.0

For manuscripts utilizing custom algorithms or software that are central to the research but not yet described in published literature, software must be made available to editors and reviewers. We strongly encourage code deposition in a community repository (e.g. GitHub). See the Nature Research [guidelines for submitting code & software](#) for further information.

### Data

Policy information about [availability of data](#)

All manuscripts must include a [data availability statement](#). This statement should provide the following information, where applicable:

- Accession codes, unique identifiers, or web links for publicly available datasets
- A list of figures that have associated raw data
- A description of any restrictions on data availability

Extended protein purification protocols are available on Protocols.io (<https://www.protocols.io/groups/hao-wu-lab>). Raw cryo-EM data are available on EMPIAR under the accession numbers EMPIAR-10594 (NLRP1-DPP9) and EMPIAR-10595 (NLRP1-DPP9-VbP). The cryo-EM maps are available on the Electron Microscopy Data Bank under the accession numbers EMD-22074 (NLRP1-DPP9) and EMD-22075 (NLRP1-DPP9-VbP). The atomic coordinates are available on the Protein Data Bank under the accession numbers 6X6A (NLRP1-DPP9) and 6X6C (NLRP1-DPP9-VbP). Pymol session files and the image analysis macro are available on OSF [<http://doi.org/10.17605/OSF.IO/X7DV8>]. All other data can be obtained from the corresponding authors upon reasonable request.

## Field-specific reporting

Please select the one below that is the best fit for your research. If you are not sure, read the appropriate sections before making your selection.

- Life sciences     Behavioural & social sciences     Ecological, evolutionary & environmental sciences

For a reference copy of the document with all sections, see [nature.com/documents/nr-reporting-summary-flat.pdf](https://www.nature.com/documents/nr-reporting-summary-flat.pdf)

## Life sciences study design

All studies must disclose on these points even when the disclosure is negative.

Sample size	No sample size calculations were performed. Experiments were performed with at least 3 biological replicates for each experiment presented. This is standard to the field, and this sample size was sufficient to observe the generally high effect size and binary outcomes of these experiments, i.e. active or inactive inflammasome processing by Western blot, high/low LDH release to measure inflammatory cell death, and ASC speck formation by confocal microscopy. All sample sizes are consistent with inflammasome literature and extent of experimental conclusions.
Data exclusions	No data were excluded.
Replication	All experiments were confirmed with multiple biological replicates as detailed in Methods or Figure Legends.
Randomization	No randomization was performed, as this does not apply to the in vitro and cellular systems used throughout this study.
Blinding	Researchers were not blinded to confocal microscopy experiments, which was not necessary given the binary nature of their effect and very large effect size. An ImageJ script was used for automated quantification of ASC specks with minimal user input.

## Reporting for specific materials, systems and methods

We require information from authors about some types of materials, experimental systems and methods used in many studies. Here, indicate whether each material, system or method listed is relevant to your study. If you are not sure if a list item applies to your research, read the appropriate section before selecting a response.

### Materials & experimental systems

n/a	Involved in the study
<input type="checkbox"/>	<input checked="" type="checkbox"/> Antibodies
<input type="checkbox"/>	<input checked="" type="checkbox"/> Eukaryotic cell lines
<input checked="" type="checkbox"/>	<input type="checkbox"/> Palaeontology and archaeology
<input checked="" type="checkbox"/>	<input type="checkbox"/> Animals and other organisms
<input checked="" type="checkbox"/>	<input type="checkbox"/> Human research participants
<input checked="" type="checkbox"/>	<input type="checkbox"/> Clinical data
<input checked="" type="checkbox"/>	<input type="checkbox"/> Dual use research of concern

### Methods

n/a	Involved in the study
<input checked="" type="checkbox"/>	<input type="checkbox"/> ChIP-seq
<input checked="" type="checkbox"/>	<input type="checkbox"/> Flow cytometry
<input checked="" type="checkbox"/>	<input type="checkbox"/> MRI-based neuroimaging

## Antibodies

Antibodies used	Primary antibodies used in this study include: DPP9 rabbit polyclonal Ab (1:1000, Abcam, Ab42080), FLAG® M2 mouse monoclonal Ab (1:1000, Sigma, F3165), GAPDH rabbit monoclonal Ab (1:1000, Cell Signaling Technology, 14C10), NLRP1-CT mouse monoclonal Ab (1:1000, R&D Systems, MAB6788), CASP1 rabbit polyclonal Ab (1:1000, Cell Signaling Technology, 2225), GSDMDC1 rabbit polyclonal Ab (1:1000, Novus, NBP2-33422), V5 rabbit polyclonal Ab (1:1000, Abcam, Ab9116), HA tag rabbit monoclonal Ab (1:1000, Cell Signaling Technology, 3724). Secondary antibodies used in this study include: IRDye 680 RD Streptavidin (1:1000, LI-COR, 926-68079), IRDye 800CW anti-rabbit (1:10000, LI-COR, 925-32211), IRDye 800CW anti-mouse (1:10000, LI-COR, 925-32210), IRDye 680CW anti-rabbit (1:10000, LI-COR, 925-68073), IRDye 680CW anti-mouse (1:10000, LI-COR, 925-68072).
Validation	All antibodies used in these studies have been evaluated by our groups in previously peer-reviewed publications, including in knockout cells. In particular, GSDMD (Novus, NBP2-33422), CASP1 (Cell Signaling Technology, 2225), and DPP9 (Abcam, Ab42080) antibodies were validated in knockout cells in Johnson et. al., 2018 Nat Med, whereas the NLRP1-CT antibody (R&D systems, MAB6788) was validated in Johnson et. al 2020 Cell Death Dis. as well as through transient expression in HEK cells in this paper. The Streptavidin antibody (LI-COR, 926-68079) was validated previously (Griswold et. al, Cell Chem Bio 2019). All other antibodies have been validated extensively in peer-reviewed publications as detailed on the manufacturers' websites.

## Eukaryotic cell lines

Policy information about [cell lines](#)

Cell line source(s)	HEK293T cells stably expressing GSDMD and caspase-1 were previously described (Johnson et. al., 2018 Nat Med). DPP8/9 knockout HEK cells were generated in this study using previously validated DPP9 KO cells (Griswold et. al, 2019 ACS Chem Bio). Wild-type HEK293T (ATCC), Expi293F (ThermoFisher), and Sf9 (ThermoFisher) cells were purchased from the manufacturer.
Authentication	Cell lines were verified by manufacturer's website and Identity of these cell lines were frequently checked by their morphological features. HEK293T (ATCC) <a href="https://www.atcc.org/en/Products/All/CRL-3216.aspx">https://www.atcc.org/en/Products/All/CRL-3216.aspx</a> . Expi293F (ThermoFisher) <a href="https://www.thermofisher.com/order/catalog/product/A14527#/A14527">https://www.thermofisher.com/order/catalog/product/A14527#/A14527</a> . Sf9 (ThermoFisher) <a href="https://www.thermofisher.com/order/catalog/product/11496015">https://www.thermofisher.com/order/catalog/product/11496015</a> .
Mycoplasma contamination	Expi293F and Sf9 cells for protein production were not tested regularly for mycoplasma contamination. All other cell lines regularly tested negative for mycoplasma using the MycoAlert Mycoplasma Detection Kit (Lonza).
Commonly misidentified lines (See <a href="#">ICLAC</a> register)	No commonly misidentified cell lines are used in this study.